

# 國立交通大學

光電工程學系顯示科技研究所

碩士論文

可應用於折射率感測器的高  $Q$  值表面模態  
二維光子晶體板緣共振腔之研究



**Researches on High Quality Factor Surface  
Mode in Two-Dimensional Photonic Crystal  
Slab-Edge Microcavity for Index Sensing**

研究生：蕭逸華

指導教授：李柏聰 教授

中華民國九十八年七月

可應用於折射率感測器的高  $Q$  值表面模態  
二維光子晶體板緣共振腔之研究

Researches on High Quality Factor Surface Mode in Two-Dimensional  
Photonic Crystal Slab-Edge Microcavity for Index Sensing

研究生：蕭逸華

Student : Yi-Hua Hsiao

指導教授：李柏聰 教授

Advisor : Dr. Po-Tsung Lee

國立交通大學

光電工程學系 顯示科系研究所



Submitted to Department of Photonics and Display Institute  
College of Electrical Engineering and Computer Science  
National Chiao Tung University

In partial Fulfillment of the Requirements  
for the Degree of Master

In  
Electro-Optical Engineering

July 2009

Hsinchu, Taiwan, Republic of China

中華民國九十八年七月

# 可應用於折射率感測器的高 $Q$ 值表面模態 二維光子晶體板緣共振腔之研究

學生：蕭逸華

指導教授：李柏璵 教授

國立交通大學光電工程學系顯示科技研究所碩士班



## 摘 要

由於超小的模態體積，利用二維光子晶體共振腔應用於折射率感測器，可以比其他光學方法所製作的感應器能偵測更小的範圍。為了獲得更高的感測度與最小的可偵測折射係數，在本論文中我們首先討論典型的二維光子晶體板緣共振腔，這種板緣共振腔最大特色就是將模態聚集在表面而容易達到高感測度，利用此特性並且藉由調變不同的切面比例以及透過三維有限時域差分法，我們可以計算此共振腔的  $Q$  值與感測度。為了更進一步最佳化  $Q$  值，我們設計了異質結構的板緣共振腔，利用其模態能隙的原理，可以較平緩地將模態聚集在共振腔內，因此大幅提升了  $Q$  值，並且也降低了其所對應最小的可偵測折射係數值。

接著用半導體製程方法將實際元件製作出來，並利用共焦顯微螢光光譜系統來量測基本的雷射特性。此外並且架設氣體真空腔系統，透過注入純二氧化碳與改變不同的氣壓，來調變此元件所處的環境折射係數，經由共焦顯微螢光光譜系統來觀察共振波長的位移，以此來計算感測度與最小可偵測折射係數值，最後將量測結果討論與分析。

# **Researches on High Quality Factor Surface Mode in Two-Dimensional Photonic Crystal Slab-Edge Microcavity for Index Sensing**

**Student : Yi-Hua Hsiao**

**Advisors : Prof. Po-Tsung Lee**

**Department of Photonics & Display Institute,  
National Chiao Tung University**

## **Abstract**

The two-dimensional photonic crystal microcavity could be applied for refractive index sensing, which could detect the smaller region than another optical method due to the ultra-small mode volume. In order to obtain the higher sensitivity and smaller detectable resolution of refractive index, in this thesis, first we discuss typical two-dimensional slab-edge-mode microcavity. The merit of this type microcavity is the mode concentrating in the surface and easily to obtain high sensitivity. From this characteristic, we apply 3D finite-difference time-domain method to simulate the quality ( $Q$ ) factor and sensitivity by varied different truncated facets. In order to further optimize the  $Q$  factor, we demonstrate hetero-slab-edge microcavities. The electric field is confined gently by mode-gap effect, therefore the  $Q$  factor is increasing suddenly, and the minimum detectable refractive index is also decreasing.

And we fabricate the real device by a series of fabrication processes. The basic lasing characters are measured by micro-PL system. In addition, we build a gas chamber to change the device environment refractive index by controlling the different pressure of carbon dioxide. The sensitivity and minimum detectable refractive index could be calculated by this experiment. Finally, we will discuss and analysis these results.

## Acknowledgements

兩年的研究生涯很快就過去了，很感謝指導教授李柏聰老師兩年來的指教，老師對於我在光子晶體領域的研究當中給予了我很大的幫助，使我受益匪淺。在老師的主持下，實驗室的風格在實驗與課業上表現很認真，娛樂休閒時大家也會一起快樂地去打球，讓我這兩年過的相當充實。

特別感謝實驗室大師兄盧贊文學長，在理論、模擬、實驗、量測各個方面給的超級專業與權威性的建議，並且對於口頭報告的邏輯思維，以及投影片、論文的製圖美學給我的超細膩與龜毛的要求和訓練，讓我這輩子受用無窮。在碩一什麼都不太懂的時候，很感謝林孟穎學姐、施均融學長、蔡宜育學長在製程與模擬上面的指導，讓我順利傳承了學長姐的經驗，快速上手製程機台。

也很感謝同組的戰友何韋德同學，除了在製程上面幫了很大的忙以外，在這碩士班兩年當中從 OPT、CLEO、以及畢業論文和口試，每次都一起奮鬥與加班，一次又一次地一起完成挑戰。感謝年紀比我大的學弟佐哥林品佐，也幫忙了我很多的實驗，祝福你以後 Ebeam 能越寫越準而且越圓，承先啟後繼往開來。也感謝學長張資岳、張明峰、王明璽、宋和聰、江俊德、蔡家揚及郭總郭光揚，學弟蕭君源、張鈞隆、蔡宜恆、鄭又瑋，同學林怡先、李欣育、洪青樺，高中同學、大學的好朋友、以及親愛的家人，感謝大家，因為你們讓我在碩士的兩年生涯不會感覺孤單，可以圓滿成功地完成碩士學位。

最後再一次感謝親愛的家人一路地支持與鼓勵，感謝所有在這兩年我所見所聞與影響我的人，謝謝所有幫忙我的人，因為這些我所感謝的人，才能交織成我這輩子很難忘、快樂充實的兩年。

蕭逸華。2009 年 8 月 謹誌於 新竹交通大學交映樓

# Content

---

<b>Abstract (In Chinese)</b> .....	<b>I</b>
<b>Abstract (In English)</b> .....	<b>II</b>
<b>Acknowledgements</b> .....	<b>III</b>
<b>Content</b> .....	<b>IV</b>
<b>Figure Captions</b> .....	<b>VI</b>
<b>Table Caption</b> .....	<b>IX</b>
Chapter 1 Introduction .....	1
1.1 Optical Index Sensor .....	1
1.2 Surface Wave in Dielectric Photonic Crystal .....	3
1.3 Background and Motivation .....	5
1.4 Overview .....	8
Chapter 2 High Q Surface Wave in PhC Slab-Edge Microcavity .....	9
2.1 Introduction .....	9
2.2 Surface Wave in PhC Slab Edge .....	10
2.2.1 Plane Wave Expansion Method .....	10
2.2.2 Analysis of Surface Wave in PhC Slab Edge by PWE Method.....	11
2.3 Typical Slab-Edge-Mode Microcavity .....	14
2.3.1 Finite-Difference Time-Domain Method.....	14
2.3.2 Analysis of Typical SLEM Microcavity by FDTD Method .....	16
2.4 Hetero-Slab-Edge (HSE) Microcavity .....	22
2.4.1 Photonic Crystal Hetero-Structure .....	22
2.4.2 HSE Microcavity Formed by Two Different $\tau$ .....	24
2.4.3 HSE Microcavity Formed by Three Different $\tau$ .....	26
2.4.4 Gradual Barrier HSE Microcavity.....	28
2.5 Conclusion .....	32
Chapter 3 Fabrications, Measurements .....	33
3.1 Introduction .....	33
3.2 Measurement Setup .....	40
3.2.1 The micro-PL system .....	40
3.2.2 Gas chamber setup .....	41
3.3 Measurement Results .....	43
3.3.1 Measurement Results from Typical SLEM Microcavity.....	43
3.3.2 Measurement Results from HSE Microcavity Formed by Two	

Different $\tau$ .....	44
3.3.3 Measurement Results from HSE Microcavity Formed by Three Different $\tau$ .....	45
3.3.4 Measurement Results from Gradual Barrier HSE .....	46
3.4 PhC HSE microcavity for Index Sensing.....	48
3.5 Conclusion.....	51
Chapter 4 Conclusions and Future Work.....	52

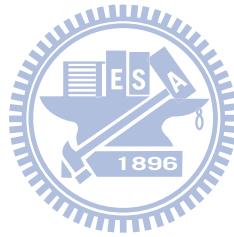


## Figure Captions

<b>Figure 1.1</b>	Scheme of 2D truncated PhC slab surrounded by air and the confinement of slab-edge.....	3
<b>Figure 1.2</b>	(a) PhC hetero-structure microcavity with air slot. (b) Electric field intensity profile of this cavity. (Adopted from reference [7]).....	6
<b>Figure 1.3</b>	(a) The SEM image and (b) the mode profile of the point-shifted nanocavity. (c) Device soaked in liquids whose refractive index ranged from 1.00 to 1.37. Obvious, there are wavelength shift when the refractive index changing. (Adopted from reference [8]) .....	6
<b>Figure 2.1</b>	Scheme of 2D truncated PhC slab surrounded by air and the definition of slab-edge termination parameter $\tau$ . .....	11
<b>Figure 2.2</b>	The calculated dispersion curves of $\tau=0.2, 0.5,$ and $0.8$ . .....	12
<b>Figure 2.3</b>	The simulated normalized frequency of SLEM under different $\tau$ by PWE method. The corresponding mode profiles of $\tau=0.2, 0.5,$ and $0.8$ are also shown in the right insets.....	13
<b>Figure 2.4</b>	Yee cell grid of 3D FDTD method. ....	16
<b>Figure 2.5</b>	The microcavity design and confinement based on SLEM. ....	16
<b>Figure 2.6</b>	The simulated mode profiles in electrical-field of SLEM microcavity with $\tau=(a) 0.3$ and (b) $0.8$ . We can observe more electrical-field concentration in air when $\tau=0.8$ , which leads to higher index sensitivity.....	17
<b>Figure 2.7</b>	The simulated $Q$ factor of SLEM microcavity with different $\tau$ .....	18
<b>Figure 2.8</b>	The simulated normalized frequency variation of SLEM microcavity .....	19
<b>Figure 2.9</b>	The simulated $Q$ factors of SLEM microcavity with different cavity .....	20
<b>Figure 2.10</b>	The simulated $Q$ factors of SLEM microcavity with different cavity .....	21
<b>Figure 2.11</b>	(a) The schematic of W1 PhC waveguide with lattice constant $a$ . (b) The calculated band structure of (a). The up arrow indicates the transmission region and the down arrow indicates gap region. (c) Double-hetero structure formed by different lattice $a_1$ (in region I) and $a_2$ (in region II) (d) the band structure along the waveguide direction. Photons only exist in the region II by the mode gap. (Adopted from reference [29]).....	23
<b>Figure 2.12</b>	The simulated mode profiles of (a) double-hetero structure and (c) L3 microcavity. The cross section electric field intensity of (b) double-hetero structure and (d) L3 microcavity. (Adopted from reference [29]) .....	24
<b>Figure 2.13</b>	The calculated dispersion curves of SLEM with $\tau=0.3$ and $0.35$ . .....	25
<b>Figure 2.14</b>	Scheme of PhC HSE microcavity formed by two different facets $\tau_1$ and $\tau_2$ . $L_1$ denotes cavity length. ....	26
<b>Figure 2.15</b>	(a) The simulated $Q$ factor and mode volume versus $L_1$ . (b) The simulated	



Q factor versus $\Delta\tau$ .....	26
<b>Figure 2.16</b> Scheme of PhC HSE microcavity formed by three different facets $\tau_1, \tau_2$ and $\tau_3$ . $L_1$ and $L_2$ denote the cavity length and the barrier length, respectively. ....	27
<b>Figure 2.17</b> The simulated Q factor and mode volume versus parameters (a) $L_2$ , (b) $\Delta\tau$ . ....	27
<b>Figure 2.18</b> The simulated surface mode profiles in electrical field.....	28
<b>Figure 2.19</b> (a) Scheme of HSE interface formed by different slab-edges $F_1$ and $F_2$ . (b) The calculated dispersion curves of $F_1$ and $F_2$ .....	29
<b>Figure 2.20</b> Scheme of PhC HSE microcavity. The gradual PhC barrier is formed by gradually shrinking and shifting air holes at the slab edge.....	30
<b>Figure 2.21</b> The simulated Q factor and mode volume versus parameters (a) $B$ and (b) $\Delta r/a$ . ....	31
<b>Figure 2.22</b> The simulated surface mode profile in electrical field when $L=10a$ , $B=5$ , and $\Delta r/a=0.04$ .....	31
<b>Figure 3.1</b> A illustration of epitaxial structure of InGaAsP quantum wells for membrane PhC lasers. The thickness of active region is about 220nm. .	34
<b>Figure 3.2</b> The fabrication processes of two-dimensional PhC membrane structure.	36
<b>Figure 3.3</b> (a) Top-view, (b) zoom-in-, and (c) tilted-view SEM pictures of fabricated typical SLEM microcavity with $\tau \sim 0.34$ .....	37
<b>Figure 3.4</b> The SEM pictures of 2D PhC HSE microcavity formed by two different $\tau$ , including (a) top-view, (b) zoom-in top-view of fabricated, and (c) zoom-in tilted-view of fabricated slab edge. ....	38
<b>Figure 3.5</b> The SEM pictures of 2D PhC HSE microcavity formed by three different $\tau$ , including (a) top-view, (b) zoom-in top-view of fabricated, and (c) zoom-in tilted-view of fabricated slab edge. ....	38
<b>Figure 3.6</b> SEM pictures of fabricated PhC gradual barrier HSE microcavity, including (a) tilted-view, (b) top-view of fabricated device, and zoom-in tilted-view of fabricated (c) slab edge and (d) PhC.....	39
<b>Figure 3.7</b> The configuration of micro-PL system .....	40
<b>Figure 3.8</b> The illustration of the gas chamber system.....	41
<b>Figure 3.9</b> The typical (a) L-L curve and (b) lasing spectrum of SLEM microcavity. Its threshold and SMSR can be estimated as 2.5mW and larger than 33dB. .	43
<b>Figure 3.10</b> (a) The SLEM wavelength tuning by varying the lattice constant from 520 to 550 nm. (b) The measured polarization with polarized ratio $\sim 6$ from SLEM.....	44
<b>Figure 3.11</b> (a) The L-L curve of HSE microcavity formed by two different $\tau$ and the spectrum near threshold with Lorentzian fitting. (b) The lasing spectrum	

at  $\lambda=1538$ . .....45

**Figure 3.12** (a) The L-L curve of HSE microcavity formed by three different  $\tau$  and the spectrum near threshold with Lorentzian fitting. (b) The lasing spectrum at  $\lambda=1528$ . .....46

**Figure 3.13** L-L curves and spectrum near threshold with Lorentzian fitting.....46

**Figure 3.14** (a) Lasing spectrum (curve A) near 1550 nm when pumping the cavity region (position A), and spectra (curves B,C, and D) when pumping outside the cavity region (positions B, C, D). (b) The measured polarization with polarized ratio of 8. (c) The pumping position. ....47

**Figure 3.15** (a) The HSE microcavity formed by three different truncated facets measurement results of resonance peak shift when the refractive index varied . The blue line indicates linear fitting. (b) The lasing spectra in the pressure 1 (1.24 atm) and pressure 2 (0.75 atm) conditions with Lorentzian fitting. ....49

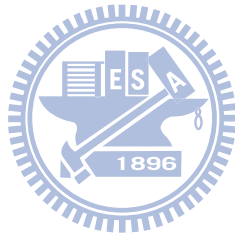
**Figure 3.16** (a) The gradual barrier HSE microcavity formed by shrinking and shifting air holes measurement results of wavelength shift in different environment index. (b) The lasing spectra of the pressure 1 (=1.13 atm) and pressure 2 (= 0.1 atm) with Lorentzian fitting. ....49



## Table Caption

---

**Table 2.1** The simulated index sensitivities and  $Q$  factor of SLEM microcavity  
with different  $\tau$ .....18



# Chapter 1 Introduction

## 1.1 Optical Index Sensor

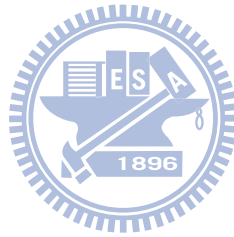
During the last two decades there is an increasing need for sensitive optical sensors in areas such as environmental control, biotechnology, chemical engineering, etc., for the measurement of chemical and biological properties. For these applications, sensors should be compact, cheap, portable, and highly sensitive. Since then a great quantity of optical methods have been developed in chemical sensors and biosensors, mainly including interferometry [1], surface plasmon resonance [2], and recently photonic crystal microcavities also have been studied extensively for sensing [3-9].

Among them, the surface plasmon resonance due to the field concentration at the surface of material, ultrahigh sensitivities in various designs have been proposed and demonstrated [10]. It has been widely applied in demonstrating various optical sensors for chemical and biological applications, for example, drug discovery, gas compositions detecting, label-free biosensing, and so on. The surface plasma wave is a charge-density oscillation that could exist at the interface of two different material. The electromagnetic wave at the interface would satisfy the following expression [2]:

$$\frac{k_{z1}}{\varepsilon_1} + \frac{k_{z2}}{\varepsilon_2} = 0 \quad (1.1)$$

where  $k_{z1}$ ,  $k_{z2}$  denote the free space wave vectors and  $\varepsilon_1$ ,  $\varepsilon_2$  the dielectric constants of the materials on the both sides, respectively. Therefore, one should be a minus number between  $\varepsilon_1$  and  $\varepsilon_2$  to satisfy equation (1.1). In the natural world, only the dielectric constant of metal is minus in visible light wavelength, so only on the surface of metal may be excited surface plasmons. Due to the field concentration at the surface of

material, the surface plasmon resonance provides extremely high sensitivities of detectable refractive index in the range of  $10^{-7}$ ~ $10^{-8}$  with detector areas of the order of  $1\text{mm}^2$ .



## 1.2 Surface Wave in Dielectric Photonic Crystal

In general, the surface plasma wave does not exist at the interface between dielectric materials. In 1966, the surface waves exist at the interface between a periodic dielectric layer and a homogeneous material that have been researched by Kossel [11]. The material with periodic index arrangement is the concept of photonic crystal (PhC) which has been proposed by E. Yablonovitch in 1987 [12]. A surface wave is defined as a propagating mode located near the interface between two material systems. The electromagnetic surface waves would propagate along the interface between the periodic structure of PhCs and air due to the photonic band gap (PBG) effect and total-internal-reflection (TIR) effect respectively. A typical 2D truncated PhC slab surrounded by air is shown in Fig. 1.1.

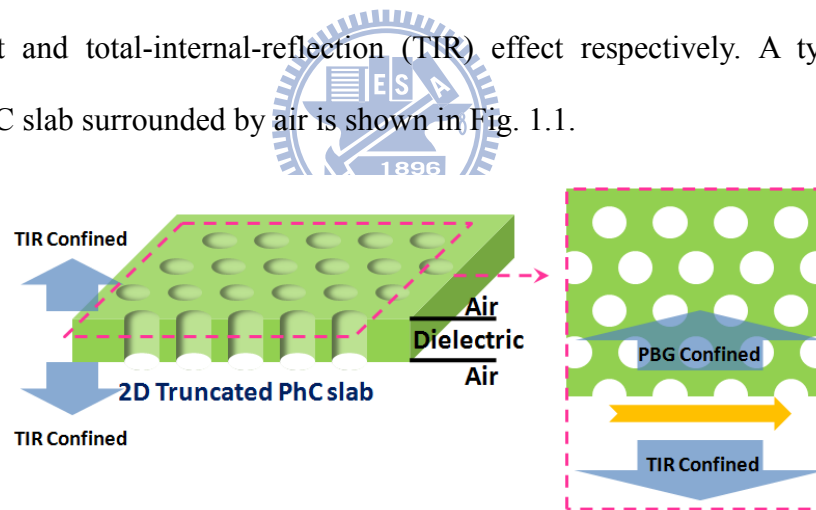


**Figure 1.1** Scheme of 2D truncated PhC slab surrounded by air and the confinement of slab-edge

Lots of interesting designs of microcavity [13-16] and waveguide [17-26] based on surface wave in 2D PhCs have been reported and which are expected as important components in constructing versatile photonic integrated circuits (PhICs). Z. Zhang et al. have proposed an optical filter based on side coupling between silicon wire

waveguide and 2D PhC surface mode cavity [16]. H. Chen et al. have demonstrated a bi-directional coupler by using a conventional dielectric waveguide side coupled to the multimode surface modes in 2D PhC waveguide [17]. E. Moreno et al. have studied the surface mode collimated emission by appropriate corrugation of the PhC interface [18]. And J. K. Yang et al. have proposed slab-edge mode microcavities in 2D PhCs by designing various PhC mirrors in truncated PhC slabs, microcavities with confined surface waves can be formed [13].

Among above designs, the optical microcavities attract lots of attentions due to the abilities of well-confining photon flow locally in a condensed size and can be easily fused with other components by side-coupling ridge waveguides [16] in PhICs, which have been initiatively demonstrated and discussed recently.



### 1.3 Background and Motivation

In general, the resonant wavelength shifts as the environmental refractive index varies. Conversely, the refractive index could be detected by measuring the wavelength shift. We can define the environmental index sensing response value  $R_n$  as  $\Delta\lambda/\Delta n$  [nm/RIU (refractive index unit)]. The detectable index variation can be obtained by inserting  $R_n$  and  $Q$  into following expression:

$$\Delta n_{\text{det}} = \frac{1}{R_n} \times \frac{\lambda}{Q} \quad (1.2)$$

where  $\lambda$  and  $\lambda/Q$  denote the wavelength and optical spectral linewidth, respectively.

Very recently, high sensitivity and condensed index sensors based on PhC defect micro- and nanocavities have been demonstrated and optimized theoretically, which show the abilities of sensing very small index variation in very condensed size. The surface plasmon resonance provides extremely high sensitivities in the range  $\Delta n_{\text{det}}=10^{-7}-10^{-8}$  but with detector areas of the order of  $1\text{mm}^2$ . By contrast, PhC nanocavity sensors tend to have lower sensitivities  $\Delta n_{\text{det}} =10^{-2}-10^{-4}$  but can be designed to fully localize the optical field to an area of  $1\ \mu\text{m}^2$ , which can be readily integrated onto a chip.

S. H. Kwon et al. have proposed a PhC hetero-structure microcavity [7] with high index sensitivity of  $512\ \text{nm} / \text{RIU}$  in simulations as shown in Fig. 1.2. In this structure, double-hetero-structure with central holes has been designed to improve  $Q$  factor as high as  $3.8 \times 10^6$ , and the corresponding  $\Delta n_{\text{det}}$  is as small as  $2.37 \times 10^{-6}$ . Beside, the air slot is designed in the waveguide center which would extend the field into air to improve sensitivity, thus the  $R_n$  value could approach 512 in simulation.



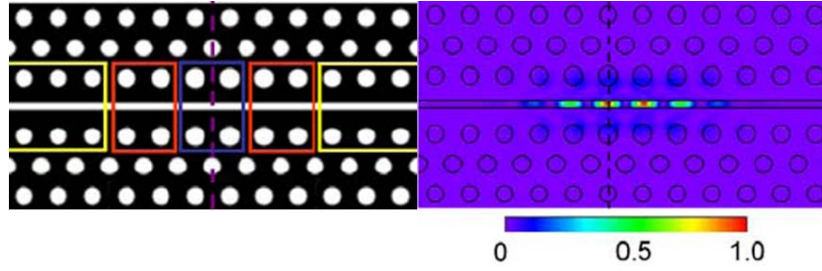


**Figure 1.2** (a) PhC hetero-structure microcavity with air slot. (b) Electric field intensity profile of this cavity. (Adopted from reference [7])

And S. Kita et al. [8] also demonstrate high index sensitivity device by point-shifted nanocavity with ultra-small mode volume in experiment as shown in Fig. 1.3. They soaked device in liquids whose refractive index ranged from 1.00 to 1.37, and obtained the maximum sensitivity of 350 nm/RIU and  $\Delta n_{\text{det}}$  of  $9.0 \times 10^{-5}$

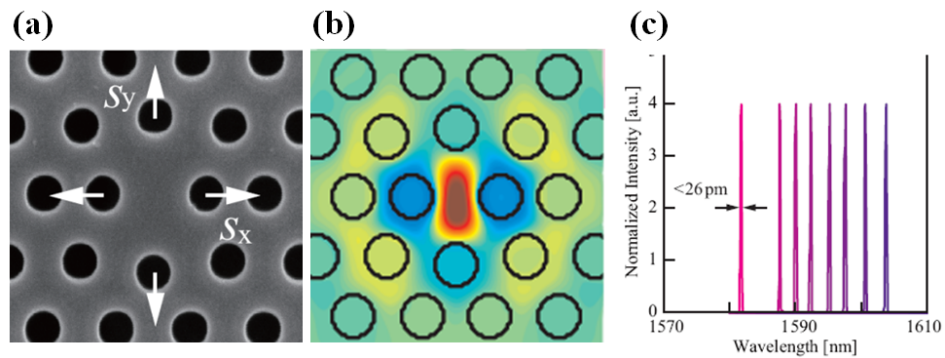
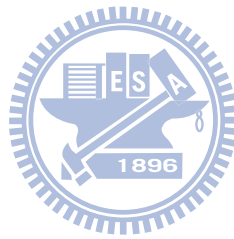


**Figure 1.3** (a) The SEM image and (b) the mode profile of the point-shifted nanocavity. (c) Device soaked in liquids whose refractive index ranged from 1.00 to 1.37. Obvious, there are wavelength shift when the refractive index changing. (Adopted from reference [8])

In these reports, in order to increase the environmental index sensing response ( $R_n$ ), the defect mode fields are extended into environmental material (air) by modifying cavity geometries. To further increase  $R_n$ , intuitively, the PhC microcavity with confined surface wave would be a very good candidate because the mode field

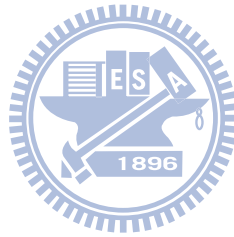
extends into environmental material, which is similar to the advantage of the high sensitivity surface plasmon resonance, and it has not been addressed and discussed in literatures. Besides, in addition to high  $R_n$  value, high quality ( $Q$ ) factor mode is also needed to provide fine optical spectral resolution and leads to high index sensitivity.

Thus, in this thesis, we propose, fabricate, and characterize a PhC slab-edge microcavity design, including typical slab-edge-mode (SLEM) microcavity, hetero-slab-edge microcavities formed by two and three different truncated facets, and gradual barrier hetero-slab-edge microcavity. The  $Q$  factor of surface mode is optimized in simulations by fine tuning the PhC patterns of the microcavity, which is aimed at achieving a high sensitivity optical index sensor.



## 1.4 Overview

In this thesis, in chapter 2, we will use finite-difference time-domain (FDTD) method and plane wave expansion (PWE) method to demonstrate the  $Q$  factor and sensitivity as environment index changing with different type and different truncated facet of surface mode microcavity. In chapter 3, the fabrication process of slab-edge mode photonic crystal microcavity structure will be illustrated. The measurement setup of micro-photoluminescence (micro-PL) system, the gas chamber setup for index sensing application, and measurement results will also be illustrated in chapter 3. And finally, we will take a brief conclusion in chapter 4.



## Chapter 2 High $Q$ Surface Wave in PhC Slab-Edge

### Microcavity

#### 2.1 Introduction

In this chapter, we focus our researches on  $Q$  factors and  $R_n$  values simulation of PhC slab-edge mode (SLEM) microcavity. At first, the fundamental properties of the surface wave propagating in PhC slab edge will be calculated by the plan-wave-expansion (PWE) method. Then, the cavity will be designed in the slab edge by adding air holes in the two sides. The  $Q$  factors and  $R_n$  values will be simulated by 3D finite-difference time-domain method (FDTD). In order to obtain the minimum detectable refractive index ( $\Delta n_{\text{det}}$ ) for sensing application, not only high sensitivities but also high  $Q$  factors are necessary. Thus, we design hetero-slab-edge (HSE) mode microcavity to obtain high  $Q$  factors. The simulated results and discussions will be shown in this chapter.

## 2.2 Surface Wave in PhC Slab Edge

### 2.2.1 Plane Wave Expansion Method

Plane wave expansion (PWE) is a useful method to calculate the band-diagram in PhC. This method is similar to the way to deal with the behavior of an electron (Krong-Penny Model) in the periodic potential in solid-state physics. Therefore, in PhC, periodic dielectric distribution can also be expanded by reciprocal lattice vector ( $\vec{G}$ ) in equation (2.1) and the wave function of photon in periodic dielectric distribution can also be expanded by the plane waves which are belong to the complete set of wave equation (2.2).

$$\text{Periodic dielectric distribution: } \epsilon(\mathbf{r}) = \sum_{\mathbf{G}} U_{\mathbf{G}} e^{i\vec{G}\cdot\vec{R}} \quad (2.1)$$

$$\text{Wave function of Photon: } \psi_{\mathbf{k}}(\mathbf{r}) = \sum_{\mathbf{G}} M(\mathbf{k} - \mathbf{G}) e^{i(\vec{k}-\vec{G})\cdot\vec{R}} \quad (2.2)$$

$$\text{Wave equation: } \frac{1}{\epsilon(\vec{r})} \nabla \times \{ \nabla \times \vec{E}(\vec{r}) \} = \frac{\omega^2}{c^2} \vec{E}(\vec{r}) \quad (2.3)$$

Finally, we substitute the equation (2.1) and (2.2) into the wave equation (2.3) in source free region from Maxwell equation, we will get new wave equation:

$$(\vec{k} + \vec{G}) \cdot (\vec{k} + \vec{G}') \times E_{G'} = -\omega^2 \sum_{G'} \epsilon_{G,G'} E_{G'} \quad (2.4)$$

This equation can be expressed as matrix form and the dispersion curve can be solved. The wavevector  $k$  is arbitrary, but can be replaced by  $k$  in the first Brillouin zone which is due to the translational symmetry inhered in PhC. Hence, we can limit our calculation in the first Brillouin zone. The  $\epsilon_{G,G'}$  is the Fourier coefficient of  $\epsilon(\mathbf{r})$  and  $\epsilon^{-1}(\mathbf{r})$ , which is concerning to  $G-G'$ . In this thesis, all the band diagrams of PhC would be calculated by this method.

## 2.2.2 Analysis of Surface Wave in PhC Slab Edge by PWE

### Method

Surface waves are propagating electromagnetic waves which are optically confined both by TIR and PBG effects at the surface of a PhC slab. The scheme of a typical 2D truncated PhC slab surrounded by air is shown in Fig. 2.1. The propagating frequency would be varied when we design different truncated facets of the air holes at the surface of the PhC slab. The PhC slab termination parameter  $\tau$  (from 0 to 1) is defined as in Fig.2.1.

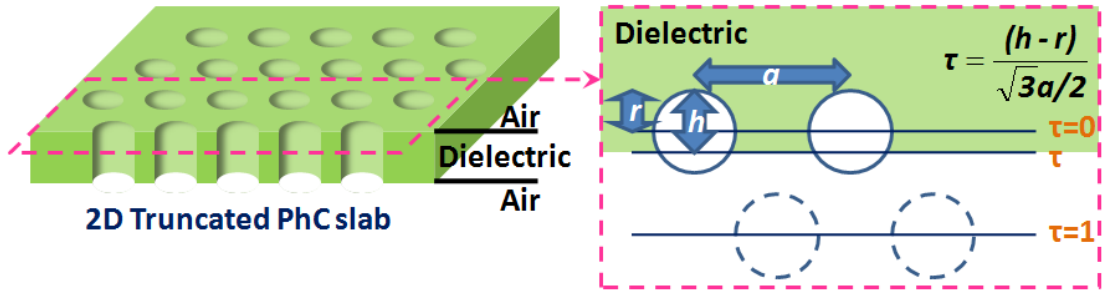


**Figure 2.1** Scheme of 2D truncated PhC slab surrounded by air and the definition of slab-edge termination parameter  $\tau$ .

In order to realize the properties of SLEM, at first, the PWE method is applied to calculate the dispersion curves in Fig. 2.2. The dielectric slab thickness and refractive index are 220nm and 3.4. The lattice constant ( $a$ ) and air-hole radius ( $r$ ) over a ( $r/a$ ) ratio are set to be 520nm and 0.37. This figure shows the dispersion characteristics of the SLEM, the dispersion curves of the SLEMs are found in the PBG region for wide range of  $\tau$ . As the wavevector near to the band edge, the slope of the dispersion curve would decrease to signify that the group velocity of the mode decreases. Therefore the SLEM near to the band edge is suitable for lasing. The normalize frequencies of the

PhC SLEM at the band edge are plotted with different terminations  $\tau$  in Fig. 2.3, and also shows the corresponding mode profiles of  $\tau=0.2, 0.5,$  and  $0.8$ . The magnetic fields of the SLEM are strongly confined to near the truncated slab-edge. In general, the lower normalized frequency would lead to the higher mode concentration in the high dielectric region. Therefore the frequency of SLEM decreases when  $\tau$  increases, which is due to the increased electromagnetic field concentration in the high dielectric region. In Fig. 2.3, we could anticipate that if we design SLEM microcavity structure, the highest  $Q$  factor will be found in  $\tau=0.2\sim 0.3$ , which is due to the frequency in the mid-gap. We also could anticipate the highest  $R_n$  value would be found in  $\tau=0.6\sim 0.8$ , because the high frequencies are near the air band that would increase electromagnetic field concentration in the low dielectric region

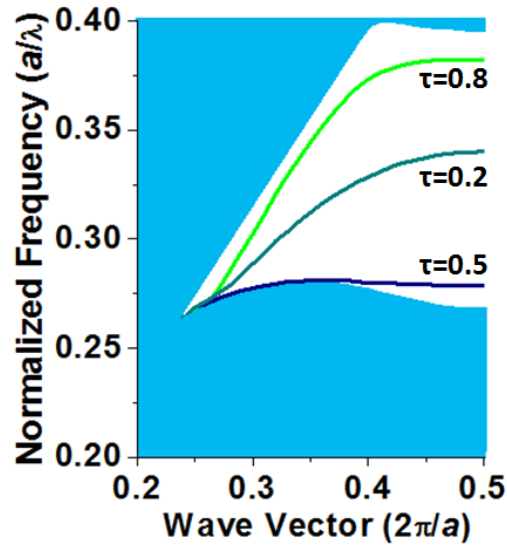


**Figure 2.2** The calculated dispersion curves of  $\tau=0.2, 0.5,$  and  $0.8$ .

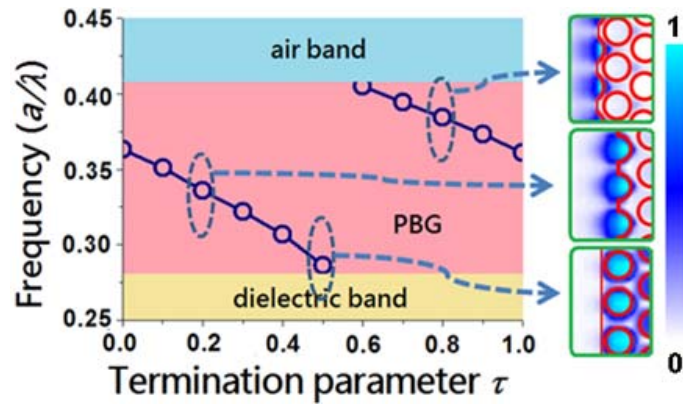
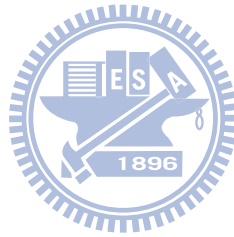


**Figure 2.3** The simulated normalized frequency of SLEM under different  $\tau$  by PWE method. The corresponding mode profiles of  $\tau=0.2$ , 0.5, and 0.8 are also shown in the right insets.





## 2.3 Typical Slab-Edge-Mode Microcavity

### 2.3.1 Finite-Difference Time-Domain Method

To simulate the behavior of electromagnetic wave in PhC, the Finite-Difference Time-Domain (FDTD) method is used most often. The FDTD method is applied to directly solve the Maxwell equation.

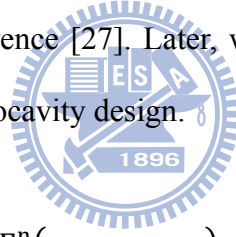
Maxwell equations are vector differential equations, but computers can only operate scalar add or subtract. Therefore, the Maxwell equations should be transformed into six scalar differential equations. FDTD method is developed to compute these six equations discretely. These six scalar differential equations for each field component of Faraday's law and Ampere's law are given by equation (2.6), where  $s$  and  $\sigma$  denote the magnetic loss and conductivity.

$$\begin{aligned}\frac{\partial E_y}{\partial z} - \frac{\partial E_z}{\partial y} &= \left( s + \mu_0 \mu_r \frac{\partial}{\partial t} \right) H_x \\ \frac{\partial E_z}{\partial x} - \frac{\partial E_x}{\partial z} &= \left( s + \mu_0 \mu_r \frac{\partial}{\partial t} \right) H_y \\ \frac{\partial E_x}{\partial y} - \frac{\partial E_y}{\partial x} &= \left( s + \mu_0 \mu_r \frac{\partial}{\partial t} \right) H_z \\ \frac{\partial H_z}{\partial y} - \frac{\partial H_y}{\partial z} &= \left( \sigma + \varepsilon_0 \varepsilon_r \frac{\partial}{\partial t} \right) E_x \\ \frac{\partial H_x}{\partial z} - \frac{\partial H_z}{\partial x} &= \left( \sigma + \varepsilon_0 \varepsilon_r \frac{\partial}{\partial t} \right) E_y \\ \frac{\partial H_y}{\partial x} - \frac{\partial H_x}{\partial y} &= \left( \sigma + \varepsilon_0 \varepsilon_r \frac{\partial}{\partial t} \right) E_z\end{aligned}$$

(2.6)

For PhC simulation, the refractive index distribution is not uniform and may be dependent on the positions. Hence, in order to describe the distribution of the

refractive index, all spaces are divided into many grids. The widely used grid form adopted in the FDTD is Yee cell as shown in Fig. 2.4. The index  $i, j, k$  denote the positions of grid points in Cartesian coordinates. The magnetic fields are centered on the facet, and the electric fields are arranged on the edges of the cubic, which is due to the electric fields updated are induced midway during each time step between successive magnetic fields, and conversely. Therefore, the electric and magnetic functions could be express as  $F(i \Delta x, j \Delta x, k \Delta x, n \Delta t) = F^n(x_i, x_j, x_k)$  at the  $n$ th time step, where  $\Delta x$  is the increment of length and  $\Delta t$  is the increment of time step. The six differential equations could discrete into the form as equation (2.7), and the six field components  $E_x^{n+1/2}, E_y^{n+1/2}, E_z^{n+1/2}, H_x^{n+1/2}, H_y^{n+1/2}, H_z^{n+1/2}$  at the  $n+1/2$  time step can be expressed with the field at the  $n$ th time step. The detail mathematical expression can be found in reference [27]. Later, we will use this FDTD method to realize the properties of our microcavity design.



$$\begin{aligned}
 \frac{\partial F^n(x_i, x_j, x_k)}{\partial x_i} &= \frac{F^n(x_{i+1/2}, x_j, x_k) - F^n(x_{i-1/2}, x_j, x_k)}{\Delta x} \\
 \frac{\partial F^n(x_i, x_j, x_k)}{\partial x_j} &= \frac{F^n(x_i, x_{j+1/2}, x_k) - F^n(x_i, x_j, x_{k-1/2})}{\Delta x} \\
 \frac{\partial F^n(x_i, x_j, x_k)}{\partial x_k} &= \frac{F^n(x_i, x_j, x_{k+1/2}) - F^n(x_i, x_j, x_{k-1/2})}{\Delta x} \\
 \frac{\partial F^n(x_i, x_j, x_k)}{\partial t} &= \frac{F^{n+1/2}(x_i, x_j, x_k) - F^{n-1/2}(x_i, x_j, x_k)}{\Delta t}
 \end{aligned}$$

(2.7)

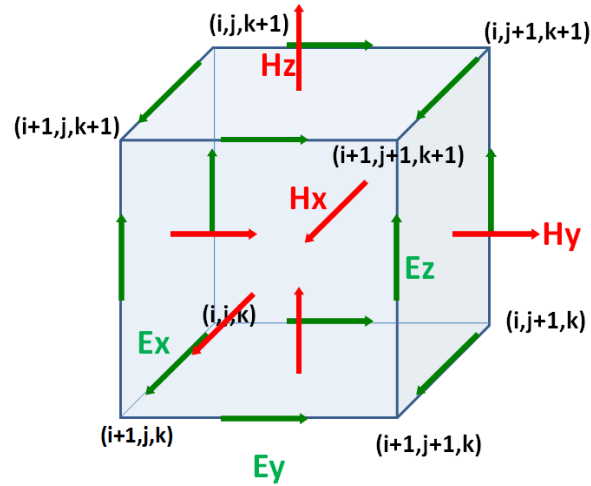


**Figure 2.4** Yee cell grid of 3D FDTD method.

### 2.3.2 Analysis of Typical SLEM Microcavity by FDTD Method

Based on the SLEM which we have discussed in Chapter 2.2, we design a microcavity by PhC slab-edge with air holes in the right-side and left-side as shown in Fig 2.5. The SLEM will be confined between the two-side air holes by PBG effect. We apply 3D FDTD simulation to investigate the SLEM in this microcavity. The lattice constant,  $r/a$  ratio, cavity length, and  $\tau$  are set to be 520 nm, 0.37, 5.1  $\mu\text{m}$ , and 0.2 to 0.8, respectively.

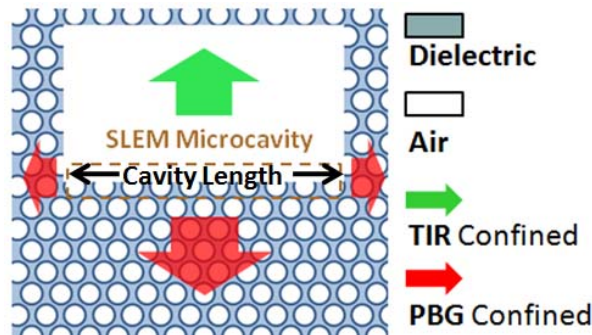


**Figure 2.5** The microcavity design and confinement based on SLEM.

The simulated mode profiles of SLEM with  $\tau=0.3$  and  $0.8$  are shown in Fig. 2.6. The right figure is the field intensity with different position along the red line in the left figure. In the right figure, the field intensity would decay in the left side of the slab-edge by TIR effect and decay in the right side of the slab-edge by PBG effect. We could observe that the field as  $\tau=0.8$  is much concentrative in air region than  $\tau=0.3$ , which is the same as our discussion in Chapter 2.2.2.

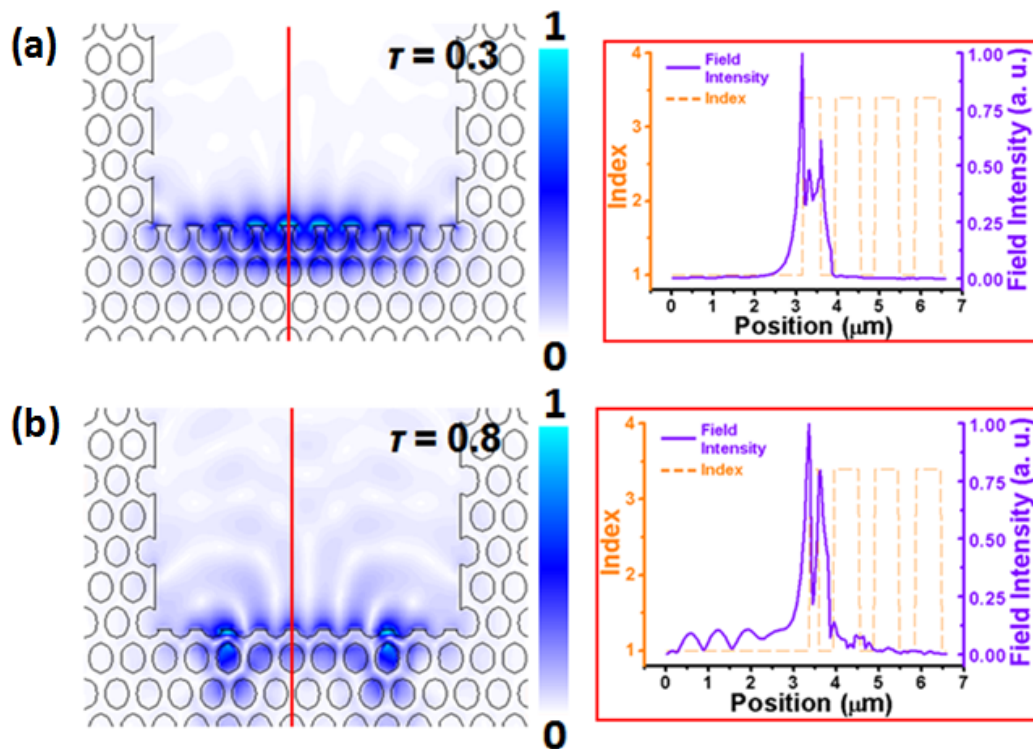


**Figure 2.6** The simulated mode profiles in electrical-field of SLEM microcavity with  $\tau=$  (a)  $0.3$  and (b)  $0.8$ . We can observe more electrical-field concentration in air when  $\tau=0.8$ , which leads to high index sensitivity.

Then, we calculate the  $Q$  factor of SLEM with different  $\tau$  and find the highest and lowest  $Q$  factors of  $1,021$  and  $112$  when  $\tau=0.3$  and  $0.8$ , as shown in Fig. 2.7. The former and latter values are attributed to the SLEM frequencies that lie in mid-gap and edge of the PBG, respectively, as shown in Fig 2.3.

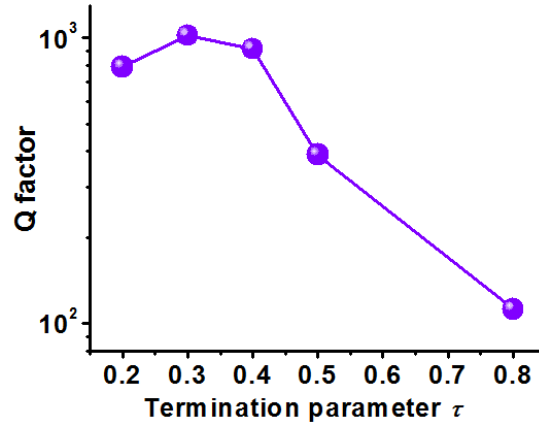


**Figure 2.7** The simulated  $Q$  factor of SLEM microcavity with different  $\tau$

We also calculate the SLEM modal frequency variation of microcavities with different  $\tau$  by varying the environmental index from 1.0 to 1.2, as shown in Fig. 2.8. We obtain index sensitivity as high as 744 nm / RIU ever reported when  $\tau = 0.8$ . This high sensitivity can be attributed to the more electrical-field concentration in the low-dielectric region as shown in the field profile in Fig. 2.6 (b). However, when considering the low  $Q$  factor of 112, the minimum detectable index variation ( $\Delta n_{\text{det}}$ ) is only 0.015. On the other hand, for higher  $Q$  factor of 1,021 in SLEM microcavity with  $\tau = 0.3$ , the index sensitivity is 610 nm / RIU. This high value is also attributed to the similar phenomenon with  $\tau = 0.8$ . The  $\Delta n_{\text{det}}$  is then estimated to be  $2.39 \times 10^{-3}$ , which is much better than the case when  $\tau = 0.8$ . The calculated results of other conditions are listed in Table 2.1. In Table 2.1, the index sensitivity decreases when  $\tau$  is varied from 0.2 to 0.5, which is mainly attributed to the less electrical-field concentration in the low-dielectric region.

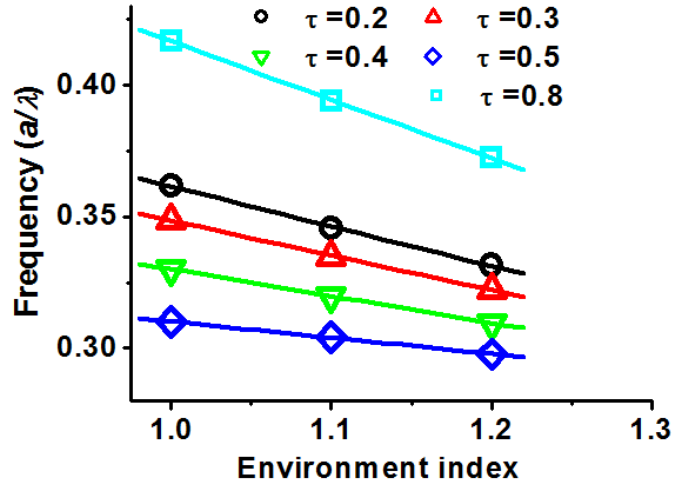


**Figure 2.8** The simulated normalized frequency variation of SLEM microcavity with different  $\tau$  when the environmental index is varied from 1.0 to 1.2

$\tau$	$Q$ Factor	Sensitivity (nm/RIU)	$\Delta n_{\text{det}}$
0.2	794	656	$2.76 \times 10^{-3}$
0.3	1021	610	$2.39 \times 10^{-3}$
0.4	916	520	$3.30 \times 10^{-3}$
0.5	390	344	$1.25 \times 10^{-2}$
0.8	112	744	$1.50 \times 10^{-2}$

**Table 2.1** The simulated index sensitivities and  $Q$  factor of SLEM microcavity with different  $\tau$ .

From the results in Table 2.1, we can conclude that high index sensing resolution requires both high index sensitivity and  $Q$  factor of microcavity. Thus, in order to improve the  $Q$  factor of SLEM microcavity with  $\tau = 0.3$ , the cavity length defined in Fig. 2.5 is varied from 5.1 to 5.5  $\mu\text{m}$ . From the simulated results in Fig. 2.9, we obtain high simulated  $Q$  factor of 1,429 when the cavity length is 5.2  $\mu\text{m}$ , which just equals to ten times to lattice constant. The index sensitivity then becomes 609 nm/RIU and

the  $\Delta n_{\text{det}}$  is estimated to be  $1.71 \times 10^{-3}$ . Although this value is still not small enough, the  $Q$  factor can be further optimized carefully and lead to improved  $\Delta n_{\text{det}}$ .

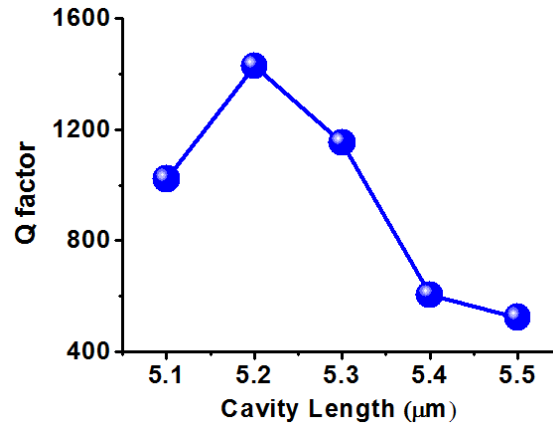


**Figure 2.9** The simulated  $Q$  factors of SLEM microcavity with different cavity length.

Beside, the  $Q$  factor of the SLEM as a function of cavity length from  $10a$  to  $15a$  is shown in Fig. 2.10. The SLEM could go through the cavity region but reflect by the right-side and left-side PhC air holes. As described in Ref. [28], for observing Fabry-Perot condition,  $Q$  factor might be enhance when the round-trip accumulated phase  $\Phi=2kL+2\Delta\phi$  is a multiple of  $2\pi$ , where  $L$  denotes cavity length and  $\Delta\phi$  denotes the phase shift from the boundary reflection. Our left-side and right-side PhC air holes are strong reflectors which could let  $\Delta\phi$  close to  $\pi$ . In Fig. 2.2, our nearly zero group velocity could be found for the wave vector  $k=0.5$  ( $2\pi/a$ ). Hence, the round-trip accumulated phase  $\Phi$  is reduced to  $(L/a)\pi+2\pi$ . Therefore, the  $Q$  factor would be enhanced when cavity length is a multiple of  $2a$ . As the cavity length increases, the  $Q$  factors will fluctuate but in average increasing which is due to the photon life time also increasing.

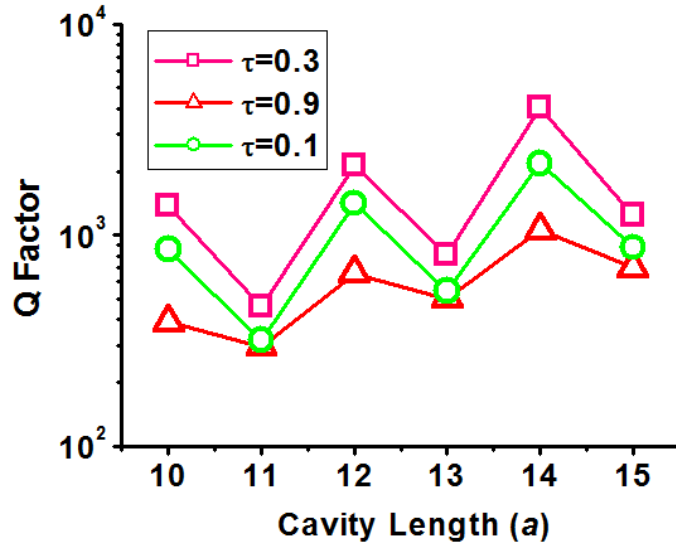


**Figure 2.10** The simulated  $Q$  factors of SLEM microcavity with different cavity lengths from  $10a$  to  $15a$  when  $\tau = 0.3, 0.9,$  and  $0.1$ .

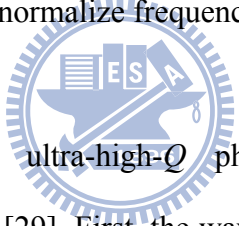
Actually, the  $Q$  factor can be increased up to larger than 10,000 by simply enlarging the cavity length to be  $20a$ . And the  $\Delta n_{\text{det}}$  will become as small as  $2 \times 10^{-4}$ . However, considering the compact device size requirement, other approaches such as gradual interface designs will be better than enlarging the microcavity in our device which will be discussed in Chapter 2.4.



## 2.4 Hetero-Slab-Edge (HSE) Microcavity

### 2.4.1 Photonic Crystal Hetero-Structure

Over the past decades, hetero-structure has been widely used in semiconductor. In semiconductor, hetero-structure can be formed by using different band-gap materials and strains. The PhC also can be formed hetero-structure by tuning some parameters in different region. Generally, the hetero-structure can be created by simply tuning the size of air holes, the position of the air holes, the lattice constant, or anything which could change the normalized frequency slightly.



B.S. Song has proposed ultra-high- $Q$  photonic double-hetero structure nanocavity as shown in Fig. 2.11 [29]. First, the waveguide mode has been simulated in a 2D PhC slab of triangular-lattice structure with a line defect waveguide formed by a missing row of air holes (W1 waveguide) as shown in Fig. 2.11 (a). The up arrow indicates the transmission region, and the down arrow indicates the mode-gap region. Then, the hetero-structures created by connecting two PhC structures I and II with different lattice constants  $a_1$  and  $a_2$ . We could observe the band diagram along the waveguide direction in Fig.2.11 (d), photons can exist only in the PhC II region by mode-gap confinement. Follow this mode-gap confinement principle,  $Q$  factors greater than  $2 \times 10^7$  may be obtained theoretically when optimizing the structure. Later, we will improve  $Q$  factor of our SLEM microcavity by this mode-gap effect.

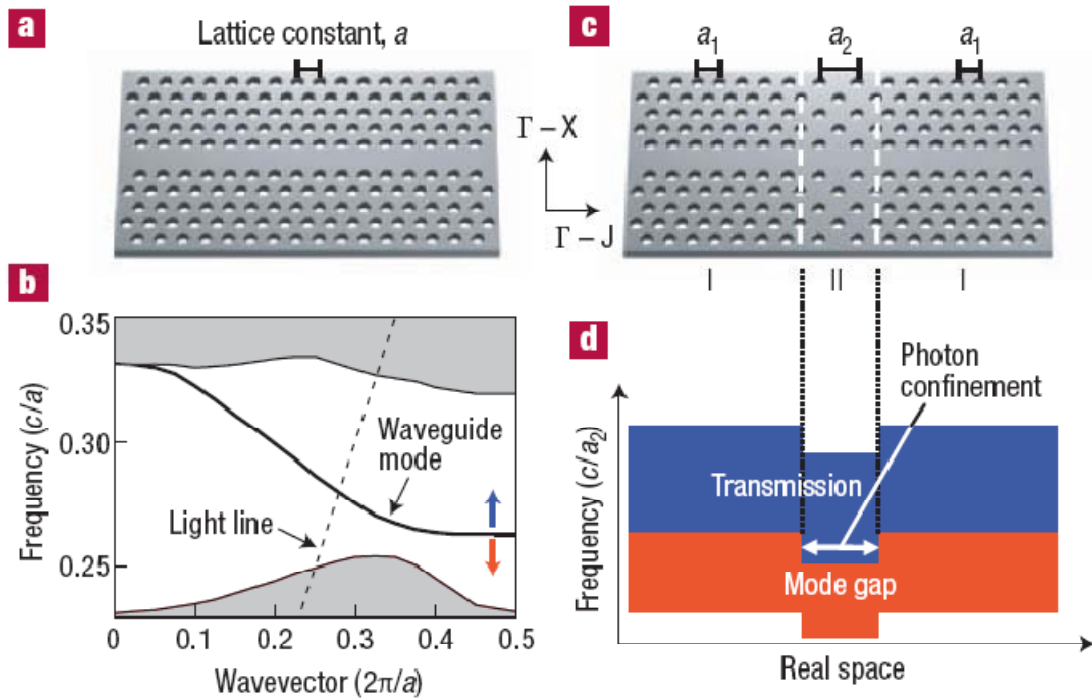


**Figure 2.11** (a) The schematic of W1 PhC waveguide with lattice constant  $a$ . (b) The calculated band structure of (a). The up arrow indicates the transmission region and the down arrow indicates gap region. (c) Double-hetero structure formed by different lattice  $a_1$  (in region I) and  $a_2$  (in region II) (d) the band structure along the waveguide direction. Photons only exist in the region II by the mode gap. (Adopted from reference [29])

The mode profile of this double-hetero structure in Fig. 2.12 (a) could be compared to triangular-lattice structure with three air holes missing and boundary modulated slightly microcavity (L3 microcavity) in Fig 2.12 (c). The cross section field intensity is shown in Fig. 2.12 (b) and (d). Obviously, the double-hetero structure is confined gently, and the cross section field intensity is much similar to Gaussian function which leads high  $Q$  factor but larger mode volume. On the contrary, the L3 microcavity is confined sharply, and the field has a large difference with Gaussian function in the cavity boundary. Therefore the  $Q$  factor is less but mode volume is smaller than the double-hetero structure.

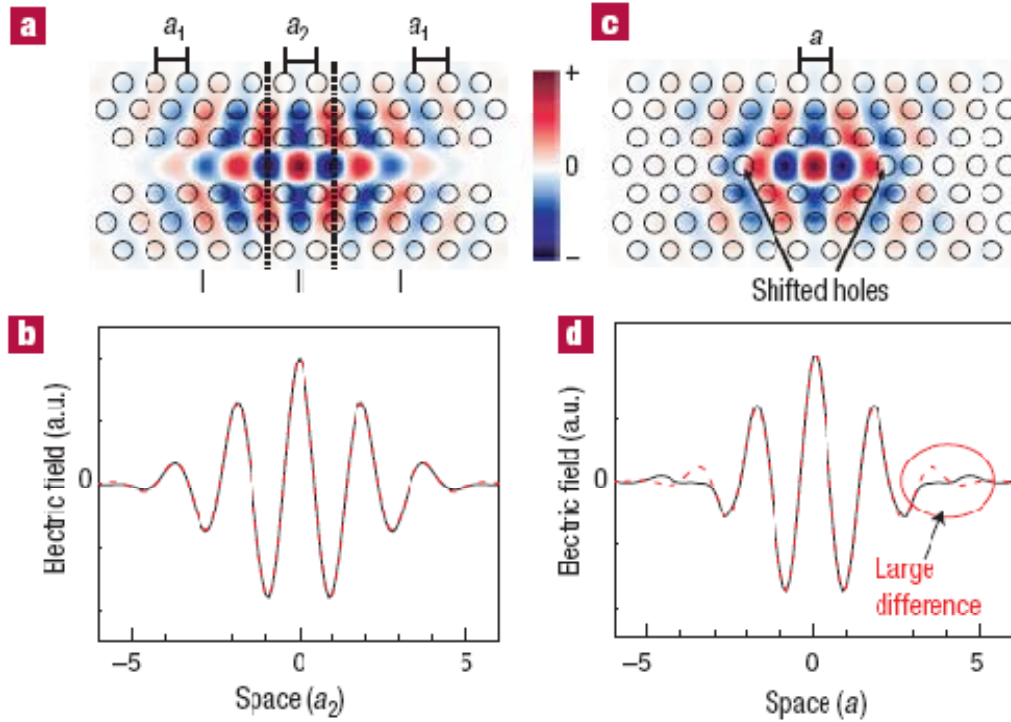


**Figure 2.12** The simulated mode profiles of (a) double-hetero structure and (c) L3 microcavity. The cross section electric field intensity of (b) double-hetero structure and (d) L3 microcavity. (Adopted from reference [29])

### 2.4.2 HSE Microcavity Formed by Two Different $\tau$

As described in Chapter 2.4.1,  $Q$  factors can be improved by hetero-structure. Here, we design the hetero-structure by different truncated facets. The dispersion curves of  $\tau=0.3$  and  $0.35$  are simulated by PWE method as shown in Fig. 2.13. There is a slight frequency shift between the bands of  $\tau=0.3$  and  $0.35$  and form the mode-gap. The light at slab-edge with  $\tau=0.3$  that lies inside the mode-gap region will regard the slab-edge with  $\tau=0.35$  as reflector.

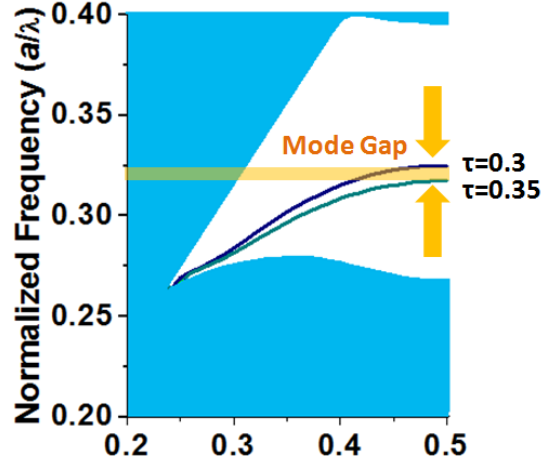


**Figure 2.13** The calculated dispersion curves of SLEM with  $\tau=0.3$  and  $0.35$ .

The cavity design of PhC hetero-slab-edge (HSE) microcavity formed by two different  $\tau$  is illustrated in Fig. 2.14. We denote the cavity length  $L_1$ , the termination parameter of cavity region  $\tau_1$ , and the termination parameter of barrier region  $\tau_2$ . The 3D FDTD method has been applied to simulate  $Q$  factors. The lattice constant  $a$ ,  $r/a$  ratio are set to be 520 nm, 0.33, respectively. First, we fix  $\tau_1=0.2a$  and  $\tau_2=0.4a$ , and tune different  $L_1$  from  $2a$  to  $10a$  to realize the relationship of  $Q$  factor and mode volume versus  $L_1$ , and which is shown in Fig 2.15 (a). The  $Q$  factor increases when the cavity length increases which is due to increasing the photon life time. But the mode volume also increases linearly as cavity length increasing. We choose  $L_1=10a$  and further optimize  $Q$  factor by tuning the  $\tau$  difference ( $\tau_2-\tau_1$ ,  $\Delta\tau$ ) as shown in Fig. 2.15 (b). The  $Q$  factor increases when the  $\tau$  difference decreases from 0.1 to 0.05. This result indicates that  $Q$  factors would be improve by gentler confinement. The  $\tau$  difference decreases from 0.05 to 0.01 which will lead  $Q$  factors decrease, because the  $\tau$  difference is smaller than the simulated resolution, and just like a SLEM waveguide that would not confine light. Finally, we obtain the highest  $Q$  factor about  $1.8 \times 10^4$  as  $\tau_2-\tau_1=0.05$ .

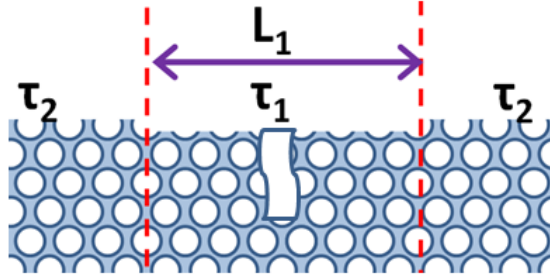


**Figure 2.14** Scheme of PhC HSE microcavity formed by two different facets  $\tau_1$  and  $\tau_2$ .  $L_1$  denotes cavity length.

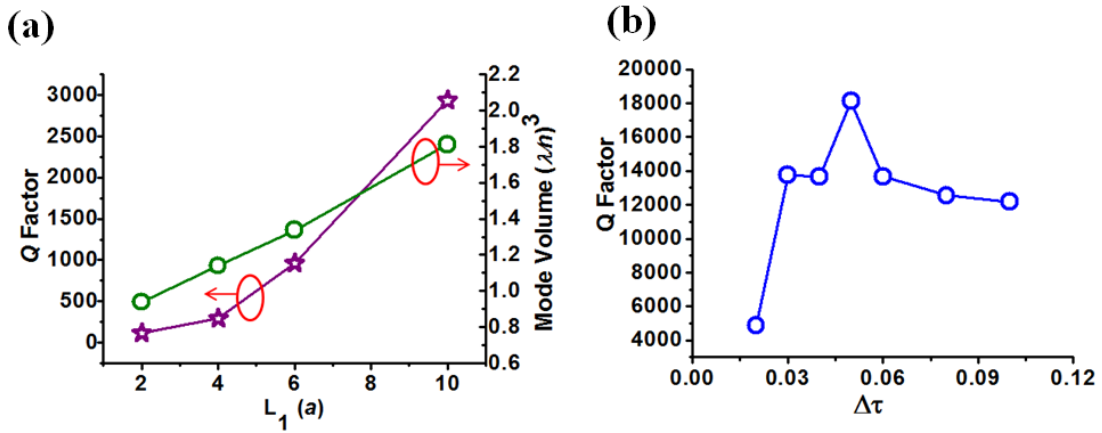


**Figure 2.15** (a) The simulated  $Q$  factor and mode volume versus  $L_1$ . (b) The simulated  $Q$  factor versus  $\Delta\tau$ .

### 2.4.3 HSE Microcavity Formed by Three Different $\tau$

We further optimize  $Q$  factor with two barriers as shown in Fig. 2.16. For the same reason in Chapter 2.4.2, light wave will confine in the cavity region by the mode-gap effect. We denote the cavity length  $L_1$ , the termination parameter of cavity region  $\tau_1$ , the barrier length  $L_2$ , the termination parameters of barrier regions  $\tau_2$  and  $\tau_3$  as shown in Fig. 2.16. The lattice constant  $a$ ,  $r/a$  ratio are set to be 520 nm, 0.33, respectively. First, we fix  $L_1=10a$ ,  $\tau_1=0.3$ ,  $\tau_2=0.35$ ,  $\tau_3=0.4$ , and the  $Q$  factors are

simulated as a function of  $L_2$  by 3D FDTD in Fig. 2.17 (a). We tune  $L_2$  from  $0a$  to  $7a$  and the highest  $Q$  Factor of  $2.2 \times 10^5$  is obtained when  $L_2 = 2a$ . If  $L_2$  is larger or smaller than  $2a$ , this structure is just like to have only one barrier which we have discussed in Chapter 2.4.2. Therefore  $Q$  factors and mode volume would decrease as  $L_2$  is larger or smaller than  $2a$ . Now,  $L_2$  is fixed to  $2a$  and the  $\tau$  difference ( $\Delta\tau = \tau_3 - \tau_2 = \tau_2 - \tau_1$ ) is tuned from 0.01 to 0.1 in Fig. 2.17 (b). We obtain high  $Q$  factor of  $5.4 \times 10^5$ , large  $R_n$  factor of 591 nm/RIU, and ultra-small  $\Delta n_{\text{det}}$  of  $4.7 \times 10^{-6}$ , when  $\tau_1 = 0.3$ ,  $\tau_2 = 0.34$ ,  $\tau_3 = 0.38$ , which is very potential in achieving highly sensitive optical index sensor. The simulated mode profile in electrical field is shown in Fig. 2.18.

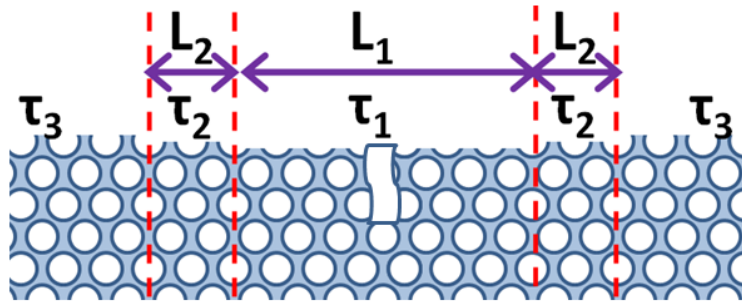


**Figure 2.16** Scheme of PhC HSE microcavity formed by three different facets  $\tau_1, \tau_2$  and  $\tau_3$ .  $L_1$  and  $L_2$  denote the cavity length and the barrier length, respectively.

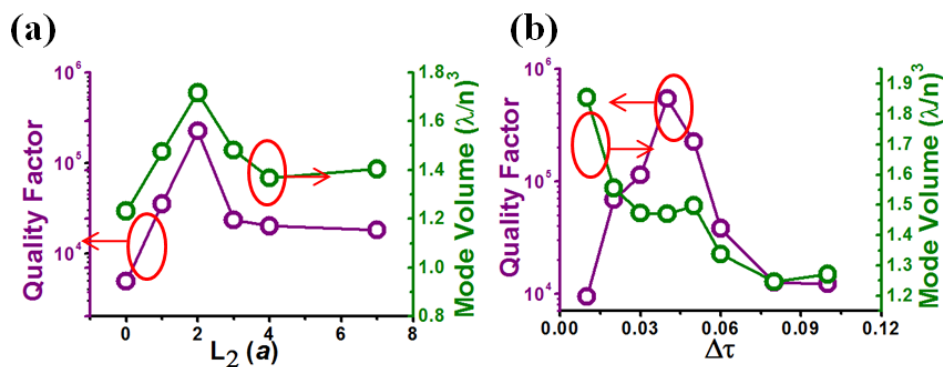


**Figure 2.17** The simulated  $Q$  factor and mode volume versus parameters (a)  $L_2$ , (b)  $\Delta\tau$ .

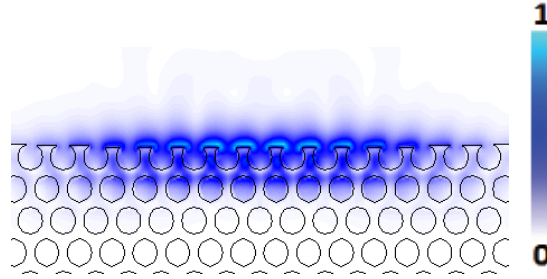


**Figure 2.18** The simulated surface mode profiles in electrical field.

#### ***2.4.4 Gradual Barrier HSE Microcavity***

To form the hetero-structure, not only different truncated facets but shrunk or shifted air holes could achieve. Here we design a barrier region by shrinking and shifting the air holes at the slab edge, which is shown and denoted as  $F_2$  in Fig. 2.19 (a). When the air holes are modified as described above, the surface mode frequency will become lower as shown in Fig. 2.19 (b). For a 2D truncated PhC HSE interface formed by slab-edges  $F_1$  and  $F_2$  shown in Fig. 2.19 (a), the surface mode with frequency inside the range indicated in Fig. 2.19 (b) will propagate in slab-edge  $F_1$  and regards the slab-edge  $F_2$  as a mirror, which forms the mode-gap effect. Thus, we can design a microcavity by applying double HSE interfaces as shown in Fig. 2.20.

In our PhC HSE microcavity design, the  $r/a$  ratios of PhC lattice [white circles in Fig. 2.20] and microcavity region (red circles) are the same (fixed  $r$  and  $a$ ) and set to be 0.36 initially. The microcavity length  $L$ , and slab thickness are set to be  $10a$  and 220 nm, respectively. The barrier region with mode-gap effect is designed by

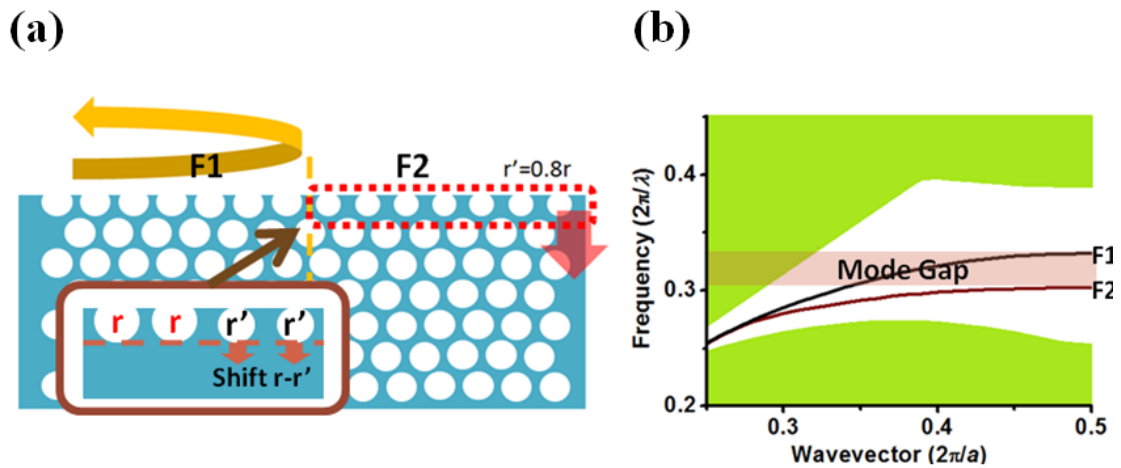


**Figure 2.19** (a) Scheme of HSE interface formed by different slab-edges  $F_1$  and  $F_2$ . (b) The calculated dispersion curves of  $F_1$  and  $F_2$ .

shrinking and shifting the air holes at the slab edge, as illustrated in Fig. 2.20. To obtain high  $Q$  microcavity, the air holes of the barrier region are shrunk and shifted gradually, from orange (number 1) to purple (number 5) circles shown in Fig. 2.20. The number of periods of the gradual barrier region is denoted as  $B$ . This gradual barrier design is mainly expected for gentle mode-gap confinement and the reduction of optical scattering losses in the barrier region. The  $r/a$  ratios of the remaining outer barrier region with purple circles in Fig. 2.20 are kept the same, and the  $r/a$  ratio difference between microcavity and outer barrier is denoted as  $\Delta r/a$ . Thus, the  $r/a$  difference between air holes in the gradual barrier region is  $\Delta r/a \times 1/B$ .

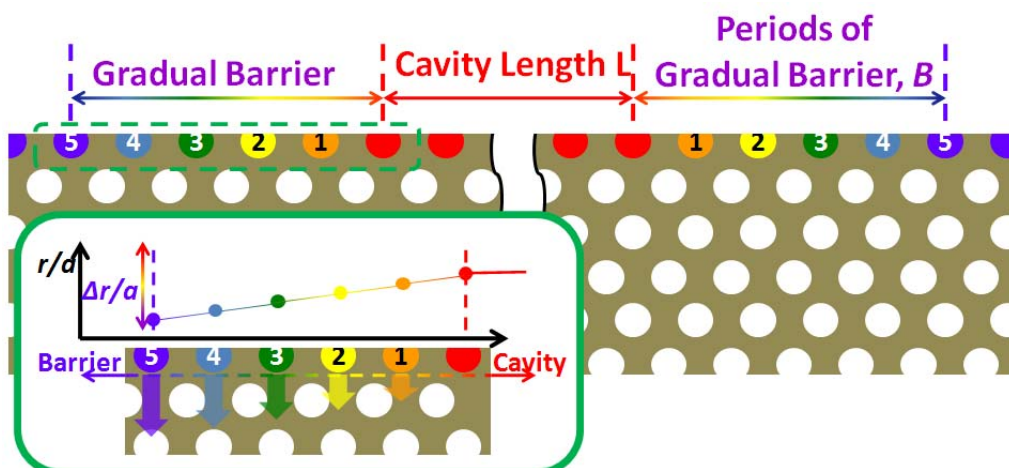




**Figure 2.20** Scheme of PhC HSE microcavity. The gradual PhC barrier is formed by gradually shrinking and shifting air holes at the slab edge.

To optimize the  $Q$  factor of PhC HSE microcavity, we vary the parameter  $B$  from 0 to 5 with  $\Delta r/a=0.03$ . The simulated  $Q$  factor and effective mode volume  $V$  by 3D FDTD simulations are shown in Fig. 2.21 (a). When  $B=0$  (no gradual barrier), the low  $Q$  factor of  $2.8 \times 10^4$  is mainly attributed to the scattering losses of the HSE interface with sharp  $r/a$  ratio variation between barrier and microcavity. Once the gradual barrier periods increase, the gentle confinement due to gentle  $r/a$  ratio variation will be provided, which leads to the increased  $Q$  factor. When  $B=5$ , the  $Q$  factor increases to  $2 \times 10^5$ . Besides, the mode volume also increases monotonically with  $B$ . This indicates the mode profile extends more into the gradual barrier region, which is caused by the gentler mode confinement. Then we further optimize the  $Q$  factor by varying  $\Delta r/a$  from 0.01 to 0.1 when  $B=5$ . The simulated results are shown in Fig. 2.21 (b). When  $\Delta r/a$  is small, the mode-gap confinement is weak and the mode will extend into the barrier, which leads to low  $Q$  factor and large mode volume. On the other hand, when  $\Delta r/a$  becomes too large, extra scattering losses are induced due to sharp mode confinement. Therefore, the  $Q$  factor is decreased and less mode profile extends into the gradual barrier region, which leads to small mode volume. Thus, we obtain an optimized high  $Q$  factor of  $6.6 \times 10^5$  when  $\Delta r/a = 0.04$  with  $V$  of  $2.25 \times (\lambda/n)^3$ . The simulated surface mode profile in electrical field is shown in Fig. 2.22. From Fig. 2.22, one can observe the significant electrical field concentrations in the air region, which implies high sensitivity of this surface mode to the environmental index variation.

To address the potential of our PhC HSE microcavity serving as a high-sensitivity index sensor, we calculated the  $R_n$  value by setting the environmental index from 1 (air) to 1.02 (with gases) in 3D FDTD simulations. The optimized HSE

microcavity design with  $Q$  factor of  $6.6 \times 10^5$  in Fig. 2.21 is applied. The calculated wavelength variation of 12.5 nm when the environmental index varied from 1 to 1.02, which corresponds to a large  $R_n$  value of 625 nm/RIU. The calculated  $\Delta n_{\text{det}}$  is as small as  $3.6 \times 10^{-6}$ . This small value actually can be further decreased by optimizing the parameter  $\tau$  and  $r/a$  ratio of PhC HSE microcavity for higher  $R_n$  and  $Q$  factor. We believe the very small  $\Delta n_{\text{det}}$  close to that of conventional interferometer can be expected and achieved by this PhC microcavity design, which is with very condensed device size.

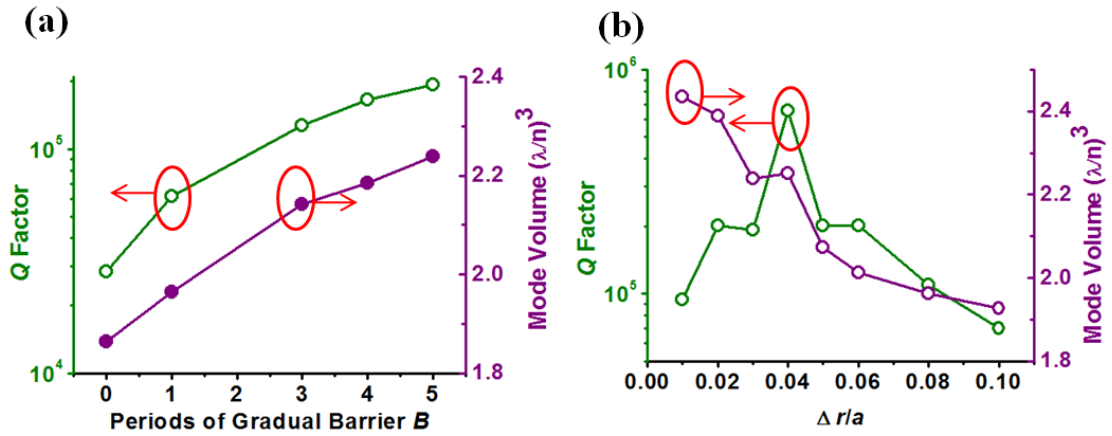


**Figure 2.21** The simulated  $Q$  factor and mode volume versus parameters (a)  $B$  and (b)  $\Delta r/a$ .

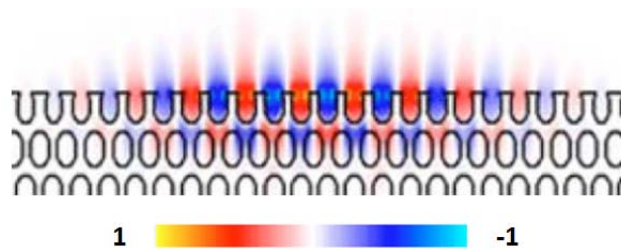


**Figure 2.22** The simulated surface mode profile in electrical field when  $L=10a$ ,  $B=5$ , and  $\Delta r/a=0.04$

## 2.5 Conclusion

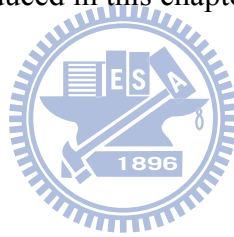
In this chapter, in order to achieve highly sensitivity optical index sensor, we design and simulate SLEM microcavity. The mode profile in electrical field of SLEM would extend to environment which is advantageous for index sensing. Therefore, we propose typical SLEM microcavity by adding air holes in the left-side and right-side of SLEM waveguide. We calculate the  $Q$  factor and  $R_n$  value of SLEM microcavity with different  $\tau$ . Highest  $Q$  factor and  $R_n$  value of 1,021 and 744 nm/RIU are obtained when  $\tau=0.3$  and 0.8, respectively. When considering the minimum  $\Delta n_{\text{det}}$  is  $2.4 \times 10^{-3}$  as  $\tau=0.3$ , which is obviously limited by the low  $Q$  factor.

To further increase the  $Q$  factor, the hetero-structure with mode-gap formed by different  $\tau$  of PhC slab-edge is applied. After a series of optimization by FDTD simulations, we obtain high  $Q$  factor of  $5.4 \times 10^5$ , large  $R_n$  value of 591 nm/RIU, and ultra-small of  $4.7 \times 10^{-6}$ , when  $\tau_1=0.3$ ,  $\tau_2=0.34$ ,  $\tau_3=0.38$ ,  $L_1=10a$ , and  $L_2=2a$ . We also propose PhC HSE with mode-gap formed by shifting and shrinking air holes. We obtain high  $Q$  factor of  $6.6 \times 10^5$ , large  $R_n$  value of 625 nm/RIU, and ultra-small  $\Delta n_{\text{det}}$  of  $3.6 \times 10^{-6}$ . With either different  $\tau$  or shifting and shrinking air holes, both hetero-structures indicate the great potential of serving as a high-sensitivity optical index sensor with very condensed device size.

## Chapter 3 Fabrications, Measurements

### 3.1 Introduction

The structures which we designed and simulated have been discussed in chapter 2. In this chapter, we will introduce the fabrication process of membrane structure PhC lasers. In order to measure the lasing characteristics and sensitivity of our fabricated devices, we use a micro-photoluminescence system and design a gas chamber, which would also introduced in this chapter.



## 3.1 Fabrication

### 3.1.1 Fabrication Process

The real devices are fabricated on an epitaxial structure consisting of four 10nm 0.85% compressively strained InGaAsP quantum wells which are separated by three 20nm unstrained InGaAsP barrier layers as shown in Fig. 3.1. The multiple quantum well layers are grown on InP substrate by metal organic chemical vapor deposition (MOCVD) and then a 60nm InP cap layer is grown on them for protecting the quantum wells during a series of dry etching processes.

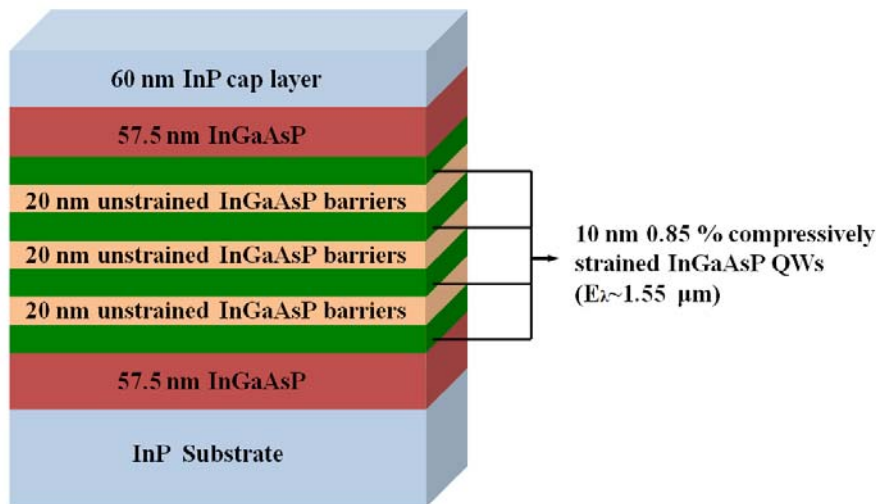


**Figure 3.1** A illustration of epitaxial structure of InGaAsP quantum wells for membrane PhC lasers. The thickness of active region is about 220nm.

Before the patterns definition, we deposited a 140 nm thick  $\text{Si}_3\text{N}_4$  layer as an etching hard mask by plasma enhanced chemical vapor deposition (PECVD) process. The 140 nm thickness  $\text{Si}_3\text{N}_4$  is good enough to let dry etching achieving the depth to 800 nm in InP/InGaAsP layer.

After the dielectric deposition, the PhC patterns are defined by electron-beam

lithography (EBL) system. The EBL system is the practice of scanning a beam of electrons in our definition pattern with a polymethylmethacrylate (PMMA) resist, and which would be selectively removed exposed regions of the PMMA resist by development process. Dosage of electron-beam is an important factor for a sample in EBL. Too large dosage would lead to enlarge itself image and also affect the exposure current of neighbors, which is called proximity effect. The proximity effect is caused by electron scattering in the PMMA resist and let the neighbor geometries distortion. Especially in the slab-edge of our device, in order to get the suitable  $\tau$  which we designed, choosing the proper electron dosage is the key point to write good patterns on sample.

For transferring PhC patterns into InP layer,  $\text{Si}_3\text{N}_4$  hard mask is etched by  $\text{CHF}_3/\text{O}_2$  mixed gas in reactive ion etching (RIE). After the patterns transfer to  $\text{Si}_3\text{N}_4$  layer, we use the  $\text{O}_2$  plasma to remove the PMMA layer. Then the patterns are further transferred to multiple quantum wells by inductively coupled plasma (ICP) dry etching with  $\text{CH}_4/\text{Cl}_2/\text{H}_2$  mixed gas at  $150^\circ\text{C}$ .

In order to fabricate the membrane structure, the InP substrate below the multiple quantum wells should be removed by using a mixture solution with  $\text{HCl}:\text{H}_2\text{O}=3:1$  at  $0^\circ\text{C}$  for 8 minutes. This process also removes the 60 nm InP cap layer on the multiple quantum wells and makes the side wall and surface of the air holes smoothly to prevent the loss caused by the roughness. Finally, the membrane structure is formed and an overview of our series fabrication processes is shown in Fig. 3.2.

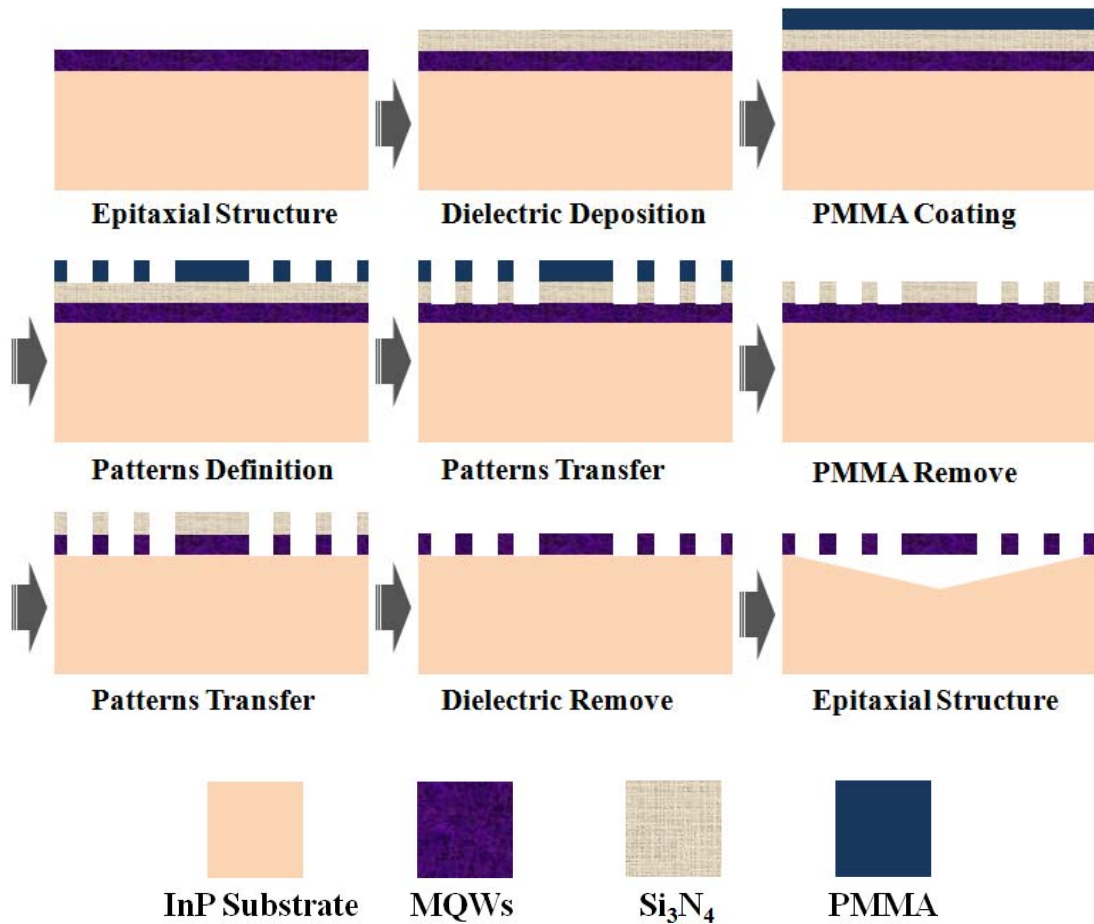


**Figure 3.2** The fabrication processes of two-dimensional PhC membrane structure.

### 3.1.2 Fabrication Result for Typical SLEM Microcavity

In this section, we demonstrated the scanning electron microscope (SEM) pictures of typical SLEM microcavity as shown in Fig. 3.3. We design a big window in the triangular lattice air holes, and the bottom of the window is our SLEM microcavity. The fabricated cavity length,  $r/a$  ratio, lattice constant, and  $\tau$  are 5.1  $\mu\text{m}$ , 0.37, 520nm, and 0.34, respectively.

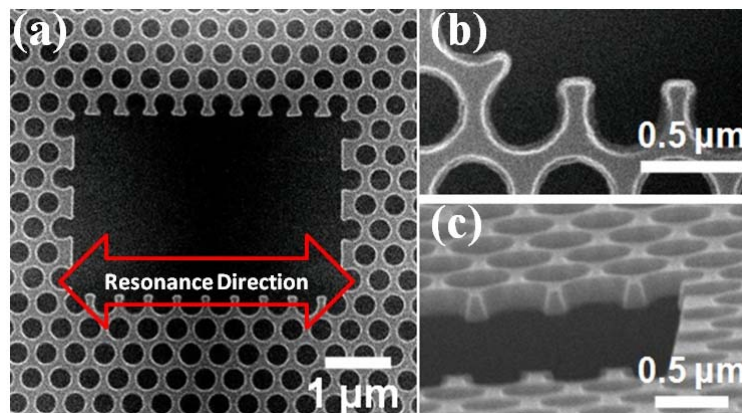


**Figure 3.3** (a) Top-view, (b) zoom-in-, and (c) tilted-view SEM pictures of fabricated typical SLEM microcavity with  $\tau \sim 0.34$

### 3.1.3 Fabrication Result for HSE Microcavity Formed by Two Different $\tau$

Following the fabrication process, we also fabricated the real device of HSE microcavity formed by different  $\tau$ . In order to obtain the suitable  $\tau$  as our designed, we fabricate the real device in array. In this array, the  $\tau$  increases from 0.27 to 0.32, the  $\tau$  difference increases from 0.02 to 0.07, the lattice constant increases from 500 nm to 530nm, and the  $r/a$  ratio equals to 0.34. In Fig 3.4, the SEM pictures show the fabricated results of HSE microcavity formed by two different  $\tau$  with  $a=500\text{nm}$ ,  $r/a$



ratio=0.34. In Fig. 3.4 (b), region 1, 2 denote the cavity region (the arrow direction, cavity length=10a), and the barrier region, respectively, which are  $\tau_1=0.27$  and  $\tau$  difference=0.02.

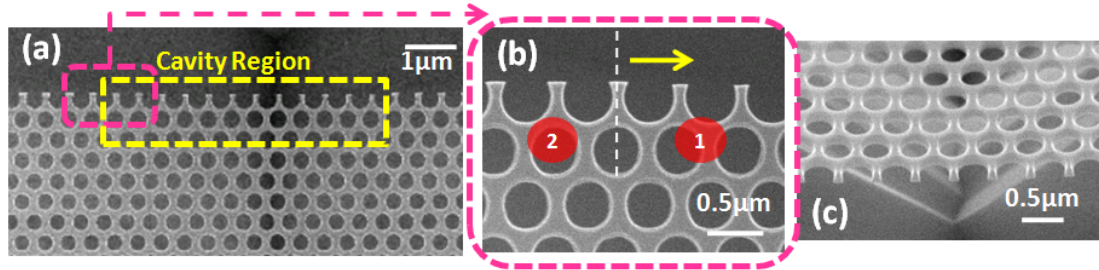


**Figure 3.4** The SEM pictures of 2D PhC HSE microcavity formed by two different  $\tau$ , including (a) top-view, (b) zoom-in top-view of fabricated, and (c) zoom-in tilted-view of fabricated slab edge.

### 3.1.4 Fabrication Result for HSE Microcavity Formed by Three Different $\tau$

The HSE microcavity formed by three different  $\tau$  is shown in Fig. 3.5, region 1, 2, 3 denote the cavity region (the arrow direction, cavity length=10a), the first barrier region, and the second barrier region, respectively, which are  $\tau_1=0.24$  and  $\tau$  difference=0.05.

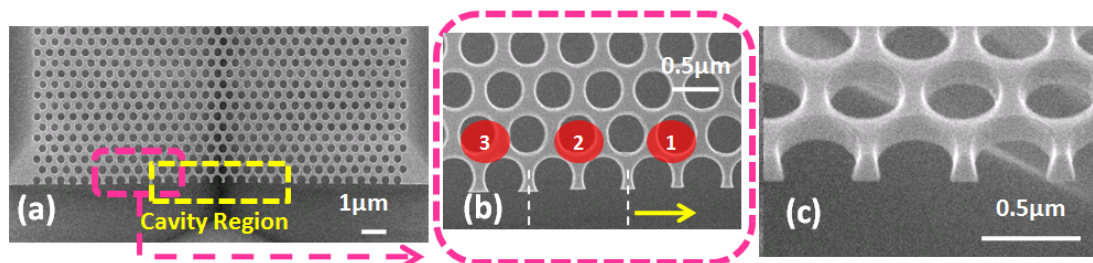


**Figure 3.5** The SEM pictures of 2D PhC HSE microcavity formed by three different  $\tau$ , including (a) top-view, (b) zoom-in top-view of fabricated, and (c)

zoom-in tilted-view of fabricated slab edge.

### 3.1.5 Fabrication Result for Gradual Barrier HSE Microcavity

We also fabricated the gradual barrier HSE microcavity formed by shrinking and shifting air holes. The SEM pictures of fabricated result are shown in Fig. 3.6. The fabricated  $\tau$ ,  $a$ ,  $r/a$ ,  $\Delta r/a$ ,  $L$ , and  $B$  are 0.24, 510 nm, 0.38, 0.08,  $10a$ , and 5, respectively.

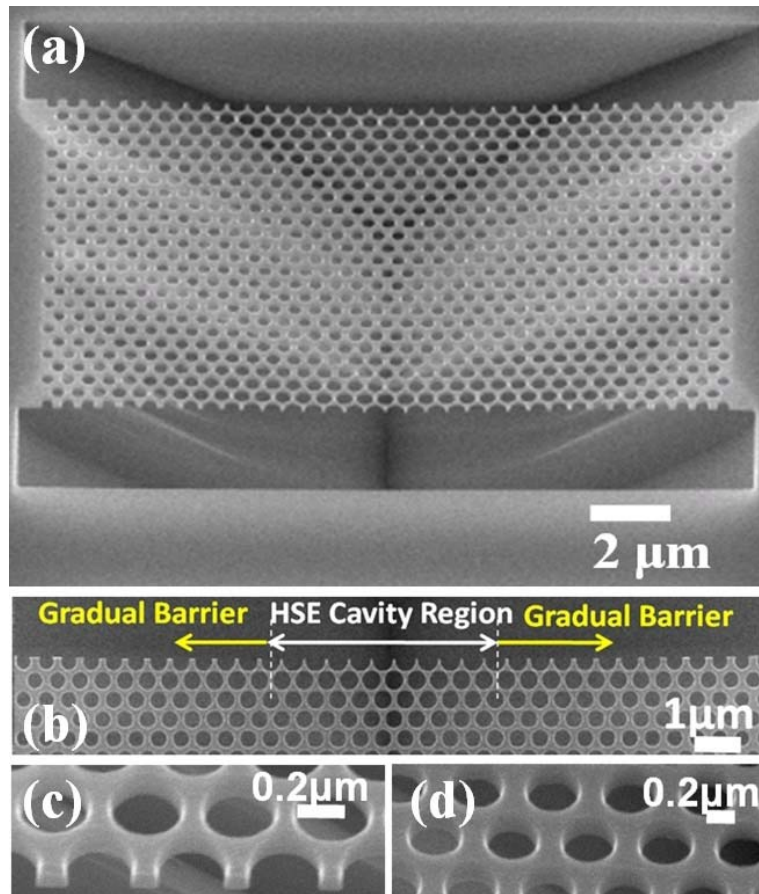


**Figure 3.6** SEM pictures of fabricated PhC gradual barrier HSE microcavity, including (a) tilted-view, (b) top-view of fabricated device, and zoom-in tilted-view of fabricated (c) slab edge and (d) PhC

## 3.2 Measurement Setup

### 3.2.1 The micro-PL system

In order to measure the characteristics of our two-dimensional PhC microcavity devices, a micro-PL system with sub-micrometer scale resolution in space and sub-nanometer scale resolution in spectrum is necessary. In this system, we use an 845 nm diode laser as the pump source. The TTL laser could be modulated in pulse operation or continuous-wave (CW) operation by a function generator. The pump beam is reflected into objective lens and focused on our sample which is mounted on a 3-axis stage. The output light from the top of the sample is collected by the objective lens, and we use a collective lens to focus the output signal into the slit of our spectrum analyzer. Therefore, we can use this system to measure the lasing spectrum of the fabricated device. The micro-PL system is shown in Fig. 3.7.

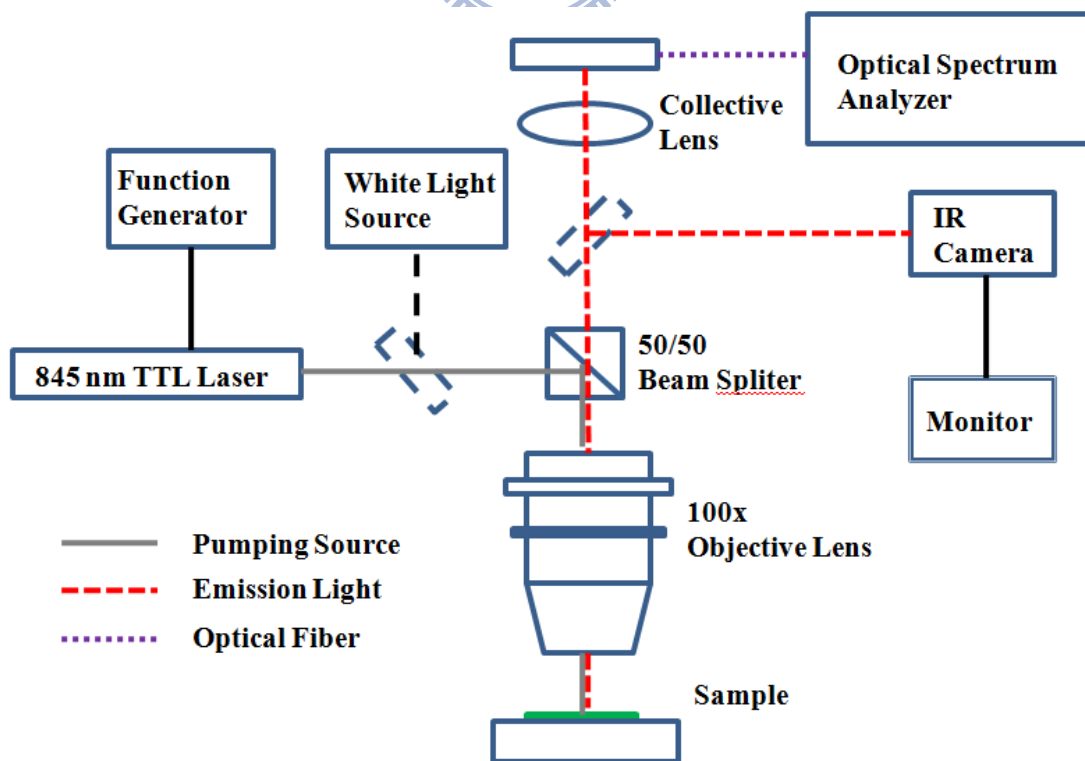


**Figure 3.7** The configuration of micro-PL system

### 3.2.2 Gas chamber setup

For index sensing application, we should put our device in different environment refractive index and measure the lasing spectrum. Gas is a better choice of the environment material than liquid, because in general the refractive index of liquid is too large and would degrade the  $Q$  factor. Therefore, a gas chamber is designed for changing the different gases and the different gas pressure. The different gases or the different gas pressure could change the different environment refractive index. The gas chamber is mounted on 3-axis stage in front of the micro-PL system which is shown in Fig 3.8. There are a vacuum port, a gas port, and a gas pressure gauge on the chamber. The chamber exhausts through the vacuum port by motor and inhales other gas through the gas port from a gas cylinder.

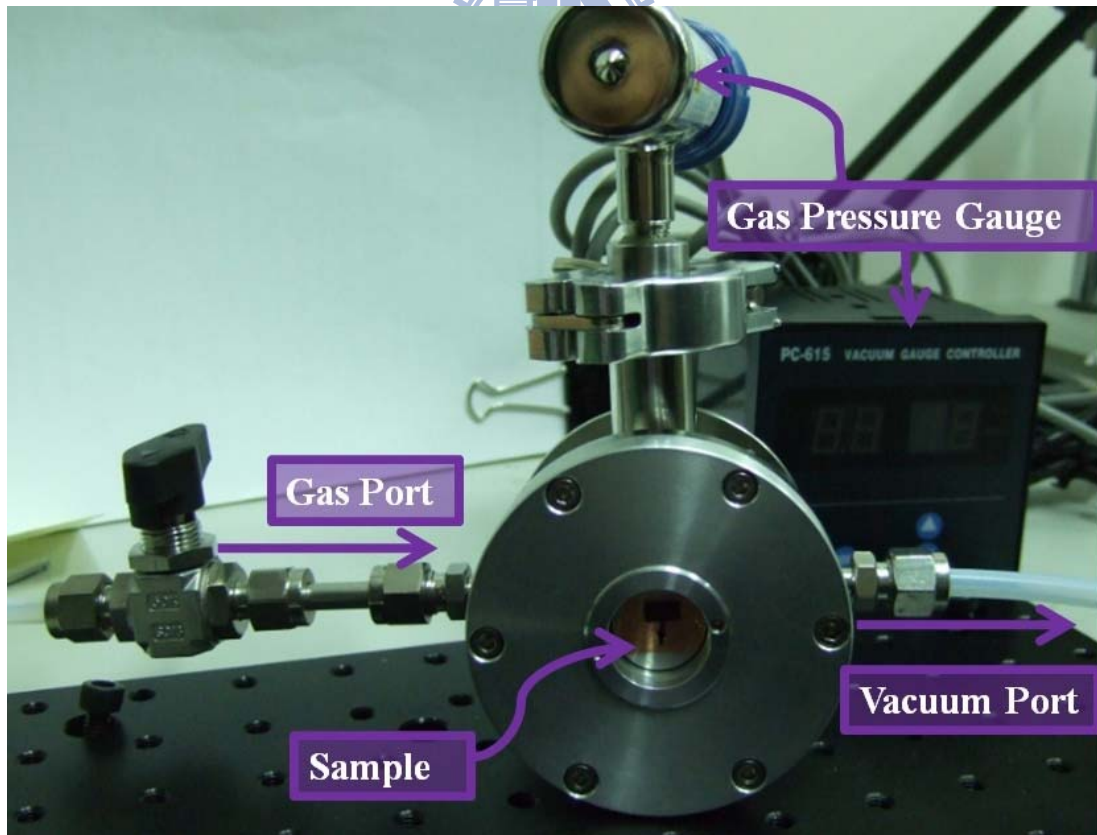


**Figure 3.8** The illustration of the gas chamber system.

We choose carbon dioxide (CO<sub>2</sub>) as environment gas, because the refractive index is larger than air, the thermal conductivity is better than air, no toxicity, very stable and without reactive on our sample. The conversion equation between the different gas pressure and refractive index for air has been proposed in 1965 [30] by Edlén which is given in the following:

$$n_{tp} - 1 = (n_s - 1) \times \frac{p[1+p(60.1-0.972t) \times 10^{-10}]}{96095.43(1+0.003661t)} \quad (3.1)$$

where  $n_{tp}$ ,  $n_s$ ,  $t$ ,  $p$  denote refractive index at this pressure and temperature condition, refractive index in 15°C and 1atm ( $n_{CO_2}=1.000449$ ), temperature (Kelvin), and pressure (Pa), respectively. We could obtain the refractive index in any assigned pressure for air. And following equation could transfer the refractive index of pure air to air containing  $x$  parts by volume of CO<sub>2</sub>:

$$(n - 1)_x = [1 + 0.540(x - 0.0003)](n - 1)_{air} \quad (3.2)$$

Above equations have been derived from measured values and the gas laws in reference [30]. We could set  $x$  of 100 % to calculate the pure CO<sub>2</sub> refractive index at any pressure. Therefore, we can calculate the sensitivity by measuring the lasing spectrum shift with different CO<sub>2</sub> pressure.

### 3.3 Measurement Results

#### 3.3.1 Measurement Results from Typical SLEM Microcavity

The SLEM microcavities with  $\tau \sim 0.34$  are optically pulse-pumped at room temperature with  $5\mu\text{m}$  pump spot size in diameter. The excitation pump spot will be located on the slab-edge, as shown in Fig. 3.3(a). The light-in light-out (L-L) curve and the lasing spectrum above threshold are shown in Fig. 3.9 (a) and (b), where the threshold and side-mode suppression ratio (SMSR) are estimated as 2.5 mW and larger than 33 dB, respectively.

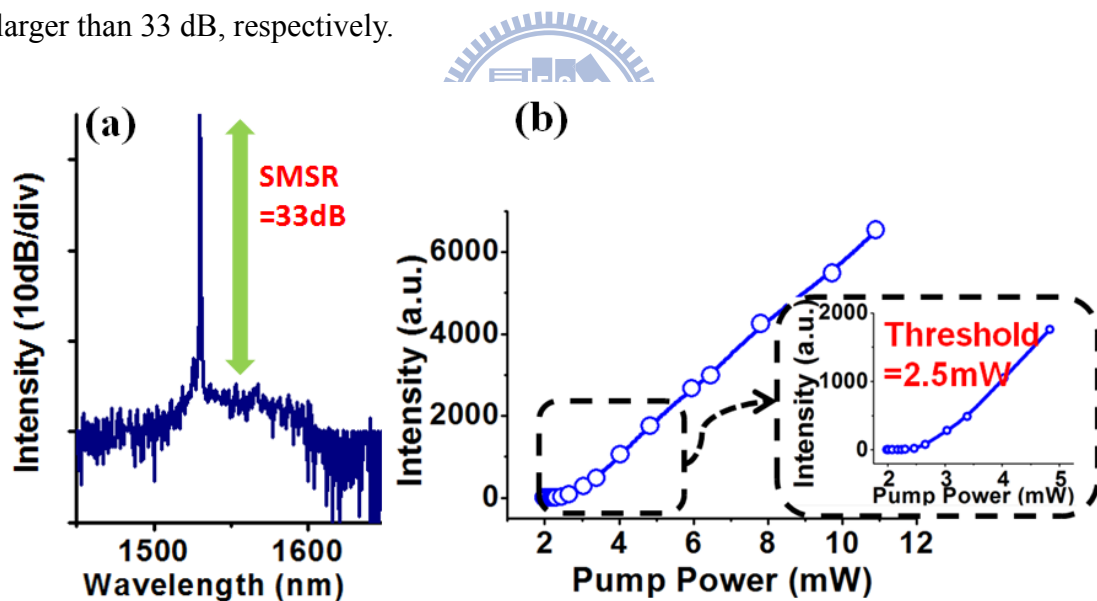


**Figure 3.9** The typical (a) L-L curve and (b) lasing spectrum of SLEM microcavity. Its threshold and SMSR can be estimated as 2.5mW and larger than 33dB.

We also show a wavelength tuning by varying the lattice constant from 520 to 550 nm with fixed  $r/a$  ratio in Fig. 3.10 (a). By comparing with the FDTD simulated

results, we can identify the lasing mode as SLEM. Besides, we also measured the polarization of the lasing mode with polarized ratio (defined as maximum over minimum collected power) of 6 by linear polarizer, as shown in Fig. 3.10 (b). This polarized light indicates that the lasing mode resonance direction is mainly parallel to the slab edge, which also provides the evidence of SLEM lasing.

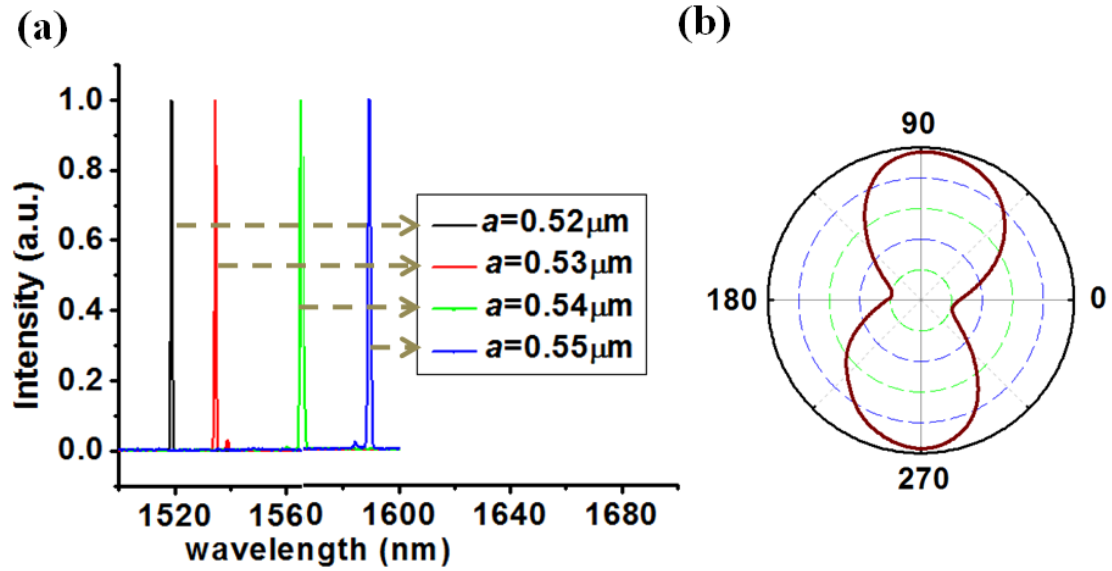


**Figure 3.10** (a) The SLEM wavelength tuning by varying the lattice constant from 520 to 550 nm. (b) The measured polarization with polarized ratio  $\sim 6$  from SLEM.

### ***3.3.2 Measurement Results from HSE Microcavity Formed by Two Different $\tau$***

The HSE microcavity formed by two different  $\tau$  is also optically pumped in cavity region. The lasing spectrum is obtained in Fig. 3.11. The threshold pump power is about 1.2 mW from L-L curve, and  $Q$  is about 5400 from the lasing spectrum near threshold with Lorentzian fitting.

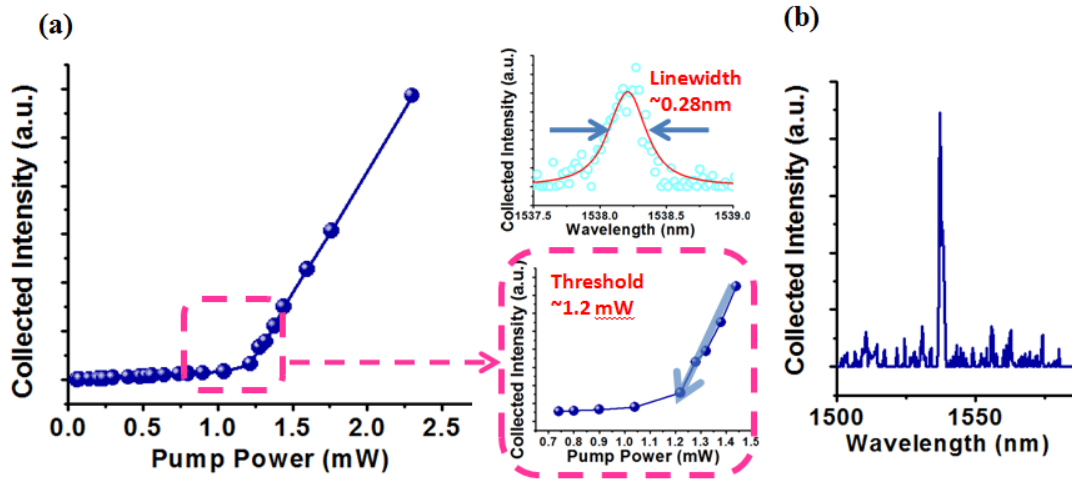


**Figure 3.11** (a) The L-L curve of HSE microcavity formed by two different  $\tau$  and the spectrum near threshold with Lorentzian fitting. (b) The lasing spectrum at  $\lambda=1538$ .

### 3.3.3 Measurement Results from HSE Microcavity Formed by Three Different $\tau$



We also optically pump the HSE microcavity formed by three different  $\tau$  in cavity region. The lasing result is obtained in Fig. 3.12. The threshold pump power is about 0.9 mW from L-L curve, and  $Q$  is about 6100 from the lasing spectrum near threshold with Lorentzian fitting. We could observe not only  $Q$  but threshold is better than the HSE microcavity formed by two different  $\tau$ .

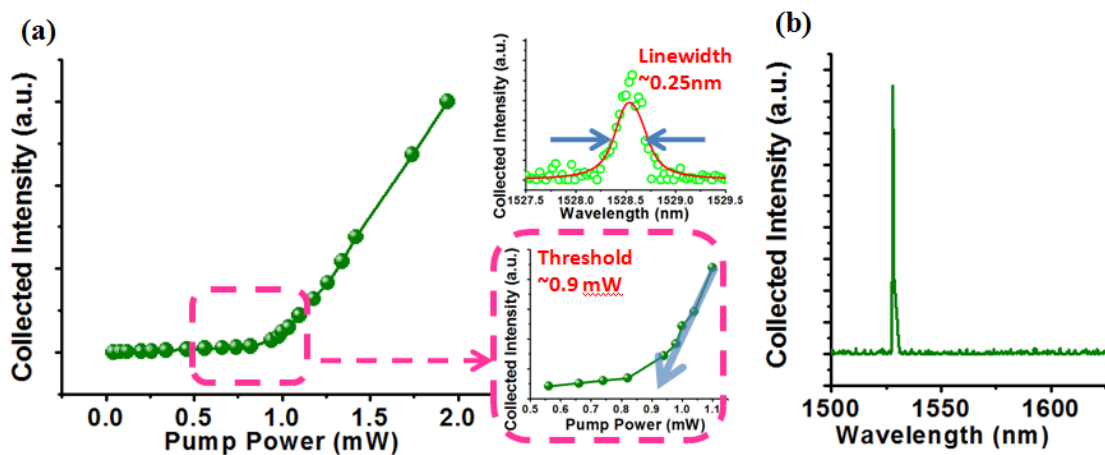




**Figure 3.12** (a) The L-L curve of HSE microcavity formed by three different  $\tau$  and the spectrum near threshold with Lorentzian fitting. (b) The lasing spectrum at  $\lambda=1528$ .

### 3.3.4 Measurement Results from Gradual Barrier HSE

The gradual barrier HSE formed by shrinking and shifting air holes are also optically pumped by a pulsed diode laser with 0.5% duty cycle at room temperature. The typical L-L curve is shown in Fig. 3.13 and the threshold is estimated to be 0.55 mW at pump position A in Fig. 3.14. The lasing spectrum near 1550 nm is shown in Fig. 3.14 (a) by curve A. The measured spectral linewidth near threshold is estimated to be 0.24 nm by Lorentzian fitting, which is shown in the inset of Fig.3.13 and corresponds to a  $Q$  factor of 6400. To further confirm light localization at the HSE microcavity, the pump position is moved outside the microcavity to positions B, C, and D (Fig. 3.14 (c)), respectively, and no lasing action is observed, as shown in Fig. 3.14 (a). Besides, the measured polarization with polarized ratio of 8 shown in the inset of Fig. 3.14 (b) also indicates the surface mode resonance along the slab edge.

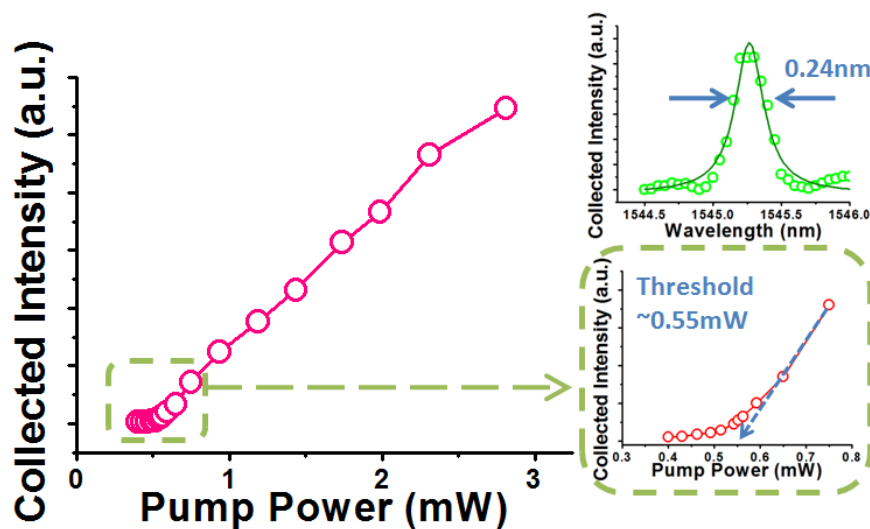


**Figure 3.13** L-L curves and spectrum near threshold with Lorentzian fitting.

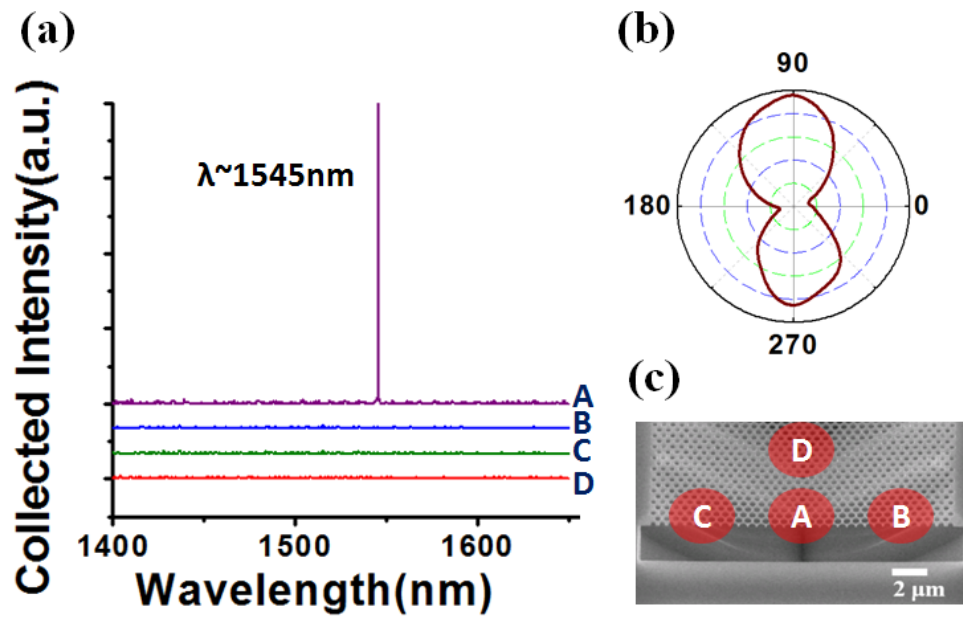


**Figure 3.14** (a) Lasing spectrum (curve A) near 1550 nm when pumping the cavity region (position A), and spectra (curves B,C, and D) when pumping outside the cavity region (positions B, C, D). (b) The measured polarization with polarized ratio of 8. (c) The pumping position.

### 3.4 PhC HSE microcavity for Index Sensing.

In this section, the real device will be put into gas chamber and measured the lasing spectrum by the micro-PL system. Air in the chamber is exhausted through the vacuum port by motor and gas pressure approached about  $10^{-4}$  atm. Then we inhale  $\text{CO}_2$  through the gas port from  $\text{CO}_2$  gas cylinder. Therefore, the  $\text{CO}_2$  gas is full of gas chamber (the pressure is a little larger than 1 atm). We start to exhaust little  $\text{CO}_2$  repeatedly and measure the resonance peak shift. The different  $\text{CO}_2$  pressure could be calculated different refractive index by equation (3.1) and (3.2).

First, we measure the HSE microcavity formed by three different truncated facets in the gas chamber as shown in Fig. 3.15 (a). The relationship about wavelength and refractive index is decreasing linearly as the refractive index decreasing. The lasing spectra of the first and last data points in Fig. 3.15 (a) are shown in Fig. 3.15 (b). In Fig. 3.15 (b), the right curve indicates the lasing spectrum with Lorentzian fitting at pressure 1 ( $=1.24$  atm,  $n=1+5.37\times 10^{-4}$ ) and the left curve indicates the lasing spectrum with Lorentzian fitting at pressure 2 ( $=0.75$  atm,  $n=1+3.25\times 10^{-4}$ ). Obviously there is a 0.29 nm blue shift as the environment condition from pressure 1 to pressure 2 which corresponds to a large  $R_n$  value of 1368 nm/RIU. The measured spectral linewidth is estimated to be 0.33 nm by Lorentzian fitting, which corresponds to a  $Q$  factor of 4706. The calculated  $\Delta n_{\text{det}}$  is as small as  $2.4\times 10^{-4}$ .

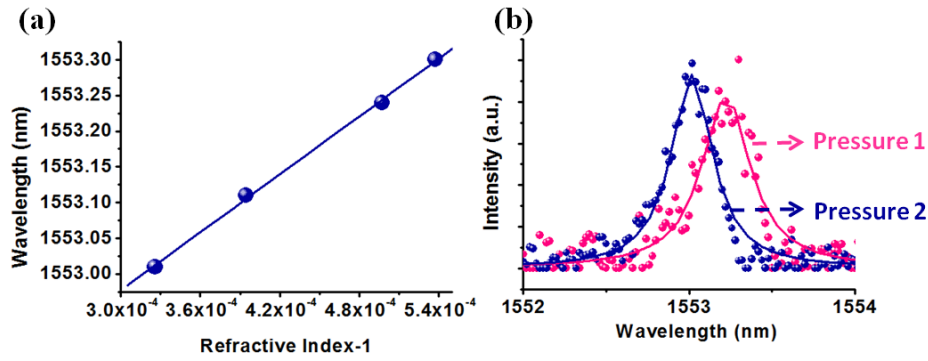


**Figure 3.15** (a) The HSE microcavity formed by three different truncated facets measurement results of resonance peak shift when the refractive index varied . The blue line indicates linear fitting. (b) The lasing spectra in the pressure 1 (1.24 atm) and pressure 2 (0.75 atm) conditions with Lorentzian fitting.

Besides, we also measure the gradual barrier HSE microcavity formed by shrinking and shifting air holes in Fig. 3.16 (a). The lasing spectra of the first and last data points in Fig. 3.16 (a) are shown in Fig. 3.16 (b). In Fig. 3.16 (b), the right and left curves indicate the lasing spectra with Lorentzian fitting at pressure 1 ( $=1.13$  atm,  $n=1+4.91\times 10^{-4}$ ) and pressure 2 ( $=0.1$  atm,  $n=1+4.46\times 10^{-5}$ ), respectively. There is a  $0.3$  nm wavelength shift which corresponds to a large  $R_n$  value of  $671$  nm/RIU. The  $Q$  factor is also obtained of  $5400$  from measured spectral linewidth about  $0.29$  nm by Lorentzian fitting and the calculated  $\Delta n_{\text{det}}$  is as small as  $4.3\times 10^{-4}$ .

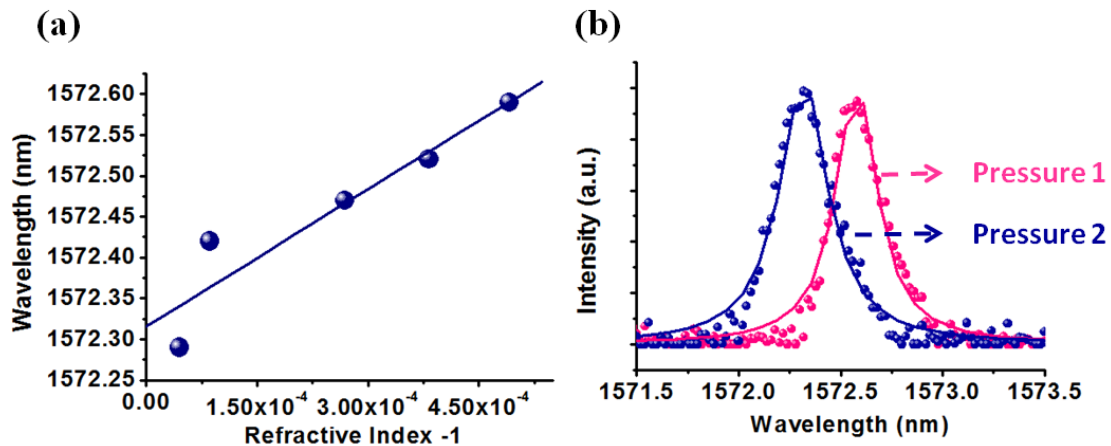


**Figure 3.16** (a) The gradual barrier HSE microcavity formed by shrinking and

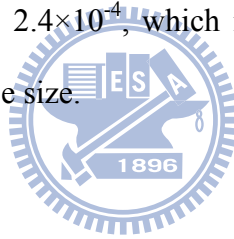
shifting air holes measurement results of wavelength shift in different environment index. (b) The lasing spectra of the pressure 1 (=1.13 atm) and pressure 2 (= 0.1 atm) with Lorentzian fitting.

We can compare these two results from Fig. 3.15 and 3.16. In the HSE microcavity formed by three different truncated facets, the  $R_n$  value of 1368 is larger than simulation results ( $R_n=591$ ), because the side wall etching of air holes is not very vertical, and field intensity would extend to air region due to the weak vertical confinement. Therefore, there is a trade-off between  $Q$  factor and  $R_n$  value, the stronger confinement would lead to the higher  $Q$  factor, but the field is also confined strongly in dielectric which would degrade  $R_n$  value. In actually, we can compare these two sensors from calculating  $\Delta n_{\text{det}}$  which means the real resolution of detectable refractive index. As above results, the  $\Delta n_{\text{det}}$  value of the HSE microcavity formed by three different truncated facets is better than the gradual barrier HSE microcavity formed by shrinking and shifting air holes, which indicates the great potential of PhC HSE microcavity serving as a high-sensitivity index sensor with very condensed device size.

### 3.5 Conclusion

In this chapter, first we introduced fabrication process. The real devices are fabricated on an epitaxial structure consisting of four 10 nm InGaAsP quantum wells by EBL and a series of RIE/ICP etching process. Then the membrane structure is formed by HCl selective wet-etching process.

After the fabrication process, the devices including typical SLEM microcavity and PhC HSE microcavity are optically pumped by a pulsed diode laser with 0.5% duty cycle at room temperature by micro-PL system. For the index sensing application, we put the real devices into gas chamber to control the different environment refractive index. The PhC HSE microcavity has been measured high  $R_n$  value of 1368 nm/RIU and  $\Delta n_{\text{det}}$  is as small as  $2.4 \times 10^{-4}$ , which is a high sensitivity optical index sensor with very condensed device size.



## Chapter 4 Conclusions and Future Work

Over the past decades, people have shown high interests in measuring material properties through various optical property variations. Recently, index sensors based on PhC have been demonstrated and could detect an area of only  $1 \mu\text{m}^2$  which have been discussed in Chapter 1. In this thesis, we propose a PhC HSE microcavity optical index sensor with high sensitivity and small detectable refractive index.

In order to obtain high  $R_n$  value, the electrical-field of resonance mode should be extended into the air. Therefore, we applied PWE method and FDTD method to simulate the properties of slab-edge mode microcavity in Chapter 2. First we discuss the typical slab-edge-mode (SLEM) microcavity with different truncated facets. We obtain the highest  $R_n$  value of 744 as  $\tau=0.8$  and the minimum  $\Delta n_{\text{det}}$  of  $2.39 \times 10^{-3}$  as  $\tau=0.3$ . But obviously, this  $\Delta n_{\text{det}}$  value is limited by the low  $Q$  factor of only 1,021. Hence, we propose high  $Q$  PhC hetero-slab-edge (HSE) microcavities formed by two and three different truncated facets, and gradual barrier formed by shrinking and shifting air holes, where the high  $Q$  surface mode is confined by mode-gap effect. By optimizing the gradual barrier in 3D FDTD simulation, we obtain high  $Q$  factor of  $6.6 \times 10^5$  from PhC gradual barrier HSE microcavity. Besides, high index sensing response  $R_n$  and small detectable index variation  $\Delta n_{\text{det}}$  of 625 nm/RIU and  $3.6 \times 10^{-6}$  are obtained in simulations. This value indicates that device could detect the variation of  $\text{CO}_2$  concentration in air about 2%.

The real devices are fabricated on an epitaxial structure consisting of four 10 nm

InGaAsP quantum wells by EBL and a series of etching process. After the fabrication process, the devices are optically pumped by a micro-PL system. There are the best measurement results of PhC gradual barrier HSE microcavity. The surface mode lasing action with high  $Q$  factor and low threshold of 6400 and 0.55 mW is obtained from the real devices.

For index sensing application, we put the real device of the HSE microcavity formed by three different truncated facets into CO<sub>2</sub> chamber. The different environmental refractive index could be varied by controlling different gas pressures. According to this method, we obtain a 0.29 nm blue shift when the pressure from 1.24 atm ( $n=5.37\times 10^{-4}$ ) to 0.75 atm ( $n=3.25\times 10^{-4}$ ), which corresponds to a large  $R_n$  value of 1368 nm/RIU and the calculated  $\Delta n_{\text{det}}$  is as small as  $2.4\times 10^{-4}$ . Both values indicate the great potential of PhC HSE microcavity serving as a high-sensitivity optical index sensor with very condensed device size, and which will be potential in applying in biological, chemical, and medical sensors in the future.

In the future, we expect our device can be applied in biological. For our active device, the  $Q$  factor will suddenly degrade when the samples are soaked in liquid. Because the index contrast between dielectric region and liquid is too small and the TIR confinement will be weak. Thus, we can demonstrate a passive device to solve this difficulty in the future. The passive device could be operated in continuous wave condition, and the  $R_n$  value could be obtained from resonance peak shift.



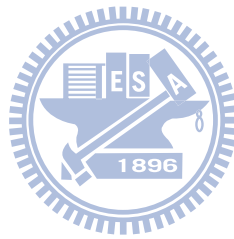
## Reference

- [1] R. G. Heideman and P. V. Lambeck, "Remote opto-chemical sensing with extreme sensitivity: Design, fabrication and performance of a pigtailed integrated optical phase-modulated Mach–Zehnder interferometer system," *Sens. Act. B*, **vol. 61**, pp. 100–127, 1999.
- [2] J. Homola, S. S. Yee, G. Gauglitz, "Surface plasmon resonance sensors: review," *Sens. Actuators B*, **vol. 54**, pp. 3-15, 1999.
- [3] M. Loncar, A. Scherer, and Y. Qiu, "Photonic crystal laser sources for chemical detection," *Appl. Phys. Lett.* **vol. 82**, pp. 4648-4650, 2003.
- [4] E. Chow, A. Grot, L. W. Mirkarimi, M. Sigalas, and G. Girolami, "Ultracompact biochemical sensor built with two-dimensional photonic crystal microcavity," *Opt. Letters*, **vol. 29**, pp. 1093-1095, 2004.
- [5] D. F. Dorfner, T. Hurlimann, T. Zabel, L. H. Frandsen, G. Abstreiter, and J. J. Finley, "Silicon photonic crystal nanostructures for refractive index sensing," *Appl. Phys. Lett.*, **vol. 93**, pp. 181103, 2008.
- [6] T. Sunner, T. Stichel, S.-H. Kwon, T. W. Schlereth, S. Hofling, M. Kamp, and A. Forchel "Photonic crystal cavity based gas sensor," *Appl. Phys. Lett.*, **vol 92**, pp. 261112, 2008.
- [7] S. H. Kwon, T. Stunner, M. Kamp, and A. Forchel, "Optimization of photonic crystal cavity for chemical sensing," *Opt. Express*, **vol 16**, pp. 11708-11717, 2008.
- [8] S. Kita, K. Nozaki, and T. Baba, "Refractive index sensing utilizing a cw photonic crystal nanolaser and its array configuration" *Opt. Express*, **vol 16**, pp. 8176-8180, 2008.

- [9] A. D. Falco, L. O'Faolain, and T. F. Krauss, "Chemical sensing in slotted photonic crystal heterostructure cavities," *Appl. Phys. Lett.*, **vol 94**, pp. 063503, 2009.
- [10] A. Lesuffleur, H. S. Im, N. C. Lindquist, and S. H. Oh, "Periodic nanohole arrays with shape-enhanced plasmon resonance as real-time biosensors," *Appl. Phys. Lett.*, **vol 90**, pp. 243110, 2007.
- [11] D. Kossel, "Analogies between Thin-Film Optics and Electron- Band Theory of Solids" *J. Opt. Soc. Am.* **vol. 56**, pp. 1434,1966.
- [12] E. Yablonovitch, "Inhibited Spontaneous Emission in Solid-State Physics and Electronics," *Phy. Rev. Lett.* **vol. 58**, pp. 2059-2062, 1987
- [13] J. K. Yang, S. H. Kim, G. H. Kim, H. G. Park, Y. H. Lee, and S. B. Kim, "Slab-edge modes in two-dimensional photonic crystals," *Appl. Phys. Lett.* **vol. 84**, pp. 3016-3018, 2004
- [14] S. Xiao and M. Qiu, "Surface-mode microcavity," *Appl. Phys. Lett.* **vol. 87**, pp. 111102, 2005
- [15] S. Xiao and M. Qiu, "Optical microcavities based on surface modes in two-dimensional photonic crystals and silicon-on-insulator photonic crystals," *J. Opt. Soc. Am. B* **vol. 24**, pp. 1225-1229, 2007
- [16] Z. Zhang, M. Dainese, L. Wosinski, S. Xiao, M. Qiu, M. Swillo, and U. Andersson, "Optical filter based on two-dimensional photonic crystal surface-mode cavity in amorphous silicon-on-silica structure," *Appl. Phys. Lett.*, **vol 90**, pp. 041108 , 2007.
- [17] H. C. Chen, K. K. Tsia, and A. W. Poon, "Surface modes in two-dimensional photonic crystal slabs with a flat dielectric margin," *Opt. Express*, **vol 14**, pp. 7368-7377, 2006.
- [18] E. Moreno, F. J. Garcia-Vidal, and L. Martin-Moreno, "Enhanced transmission

- and beaming of light via photonic crystal surface modes,” *Phys. Rev. B*, **vol 69**, pp. 121402, 2004.
- [19] W. T. Lau and S. Fan, “Creating large bandwidth line defects by embedding dielectric waveguides into photonic crystal slab,” *Appl. Phys. Lett.* **vol.81**, pp. 3915-3917, 2002
- [20] Y. A. Vlasov, N. Moll, and S. J. McNab, “Observation of surface states in a truncated photonic crystal slab,” *Opt. Lett.* **vol.29**, pp. 2175-2177, 2004
- [21] Y. A. Vlasov, N. Moll, and S. J. McNab, “Mode mixing in asymmetric double-trench photonic crystal waveguides,” *J. Appl. Phys.* **vol.95**, pp. 4538-4544, 2004
- [22] E. H. Khoo, T. H. Cheng, A. Q. Liu, J. Li, and D. Pinjala, “Transmitting light efficiently on photonic crystal surface waveguide bend,” *Appl. Phys. Lett.* **vol.91**, pp. 171109, 2007
- [23] W. Smigaj, “Model of light collimation by photonic crystal surface modes,” *Phys. Rev. B* **vol.75**, pp. 205430, 2007
- [24] H. G. Choi, S. S. Oh, S. G. Lee, M. W. Kim, J. E. Kim, H. Y. Park, and C. S. Kee, “Coupling characteristics of surface modes in truncated two-dimensional photonic crystals,” *J. Appl. Phys.* **vol.100**, pp. 123105, 2006
- [25] A. I. Rahachou and I. V. Zozoulenko, “Waveguide properties of surface states in photonic crystals,” *J. Opt. Soc. Am. B* **vol.23**, pp. 1679-1683, 2006
- [26] E. Moreno, F. J. Garcia-Vidal, and L. Martin-Moreno, “Efficient coupling of light into and out of a photonic crystal waveguide via surface modes,” *Photon. & Nanostructures: Fund. and Appl.* **vol. 2**, pp. 97-102, 2004
- [27] G. Mur, “Absorbing Boundary Conditions for the Finite-Difference Approximation of the Time-Domain Electromagnetic Field Equations,” *IEEE Transactions on Electromagnetic Compatibility.* **vol. 23**, pp. 377-382, 1981.

- [28] M. Ibanescu, S. G. Johnson, D. Roundy, Y. Fink, and J. D. Joannopoulos, “Microcavity confinement based on an anomalous zero group-velocity waveguide mode,” *Opt. Lett.*, **vol 30**, pp.552-554, 2005.
- [29] B. S. Song, S. Noda, T. Asano, and Y Akahane1, “Ultra-high-Q photonic doubleheterostructure nanocavity,” *Nature Mater.*, **vol 4**, 2005
- [30] B. Edlen, “The refractive index of air, ” *Metrologia*, **vol 2**, 1965



## Vita

**Yi-Hua Hsiao** was born on 26, May 1985 in Hsinchu City, Taiwan. He received the B.S. degree from department of engineering science in National Cheng Kung University, Tainan City, Taiwan in 2007. The M.S. degree was received from department of photonics and display institute in National Chiao Tung University, Hsinchu City, Taiwan in 2009. His researches focus on photonic crystal microcavity lasers for index sensing application.



### Publications:

- [1] Wei-De Ho, **Yi-Hua Hsiao**, Tsan-Wen Lu, Po-Tsung Lee, “Characterization of Post-Size Controlled 12-Fold Quasi-Photonic Crystal Microcavity for Electrically-Driven Structure”, *OPT*, Sat-S7-03, 2008.
- [2] **Yi-Hua Hsiao**, Wei-Te Ho, Tsan-Wen Lu, Po-Tsung Lee, “Two-Dimensional Photonic Crystal Slab-Edge Microcavity for Index-Sensing Applications with High Sensitivity”, *OPT*, Sat-S8-01, 2008.
- [3] Tsan-Wen Lu, **Yi-Hua Hsiao**, Wei-De Ho, and Po-Tsung Lee, “Photonic crystal heteroslab-edge microcavity with high quality factor surface mode for index sensing”, *Appl. Phys. Lett.* **vol.94**, pp. 141110, 2009.
- [4] **Yi-Hua Hsiao**, Tsan-Wen Lu, Wei-De Ho, Tsan-Wen Lu, Po-Tsung Lee, “High- $Q$  Photonic Crystal Hetero-Slab-Edge Microcavity Laser for Index Sensing”, *CLEO*, CTuDD4, 2009.
- [5] Wei-De Ho, **Yi-Hua Hsiao**, Tsan-Wen Lu, Po-Tsung Lee, “Thermal Properties of Post-Size Controlled 12-Fold Qasi-Photonic Crystal Microcavity for Electrically-Driving”, *CLEO*, CFE4, 2009.